ABSTRACT

An original approach to the simulation of the development of extensive air showers up to extreme energies has been conceived, developed and realized in the form of a computer code, the main features and performance of which are the subject of the present thesis. The originality of the adopted approach resides in its transparency, rapidity and flexibility, at variance with existing simulation codes that are rigid black boxes implying the use of thinning algorithms and requiring very long computer times that considerably limit the size of available samples of simulated events.

The price to pay is major simplifications and approximations of the physics mechanisms underlying the development of such showers. The approach adopted here cannot have the ambition to reproduce reality with a good accuracy, as existing sophisticated codes have. It must instead be seen as a complement to such codes with, in particular, a much stronger didactic power. It will contribute to a deeper understanding of what is really going on, to the identification of the parameters of relevance and to the evaluation of the impact of the approximations commonly made.

Extensive air showers in the extreme energy range are the manifestation of ultra high energy cosmic rays (UHECR, energies in excess of $\sim 10^{18.5}$ eV) when entering the earth atmosphere: such showers, rather than the primary nuclei that induce them, are observed by ground detectors such as the Pierre Auger Observatory in Argentina with which VATLY, the astrophysics laboratory where the present work has been made, is associated. Such observations are at the forefront of current research in the field and aim at identifying the sources (known to be extragalactic) and the nature of UHECRs and to unravel the acceleration mechanism. A first section takes stock of the current state of the art in UHECR physics and gives a brief description of the Pierre Auger Observatory, of its methods and of its present achievements.

The approach adopted here consists in describing low energy sub-showers in a parameterised form rather than following the details of their development. More precisely, the first interaction of the primary with the atmosphere is described by simulating the production of new particl1es but the interactions of such new particles with atmosphere will only be simulated when their energies exceed a predetermined fraction f, typically 5%, of the primary energy. If they do not, the new particle is simply

replaced by a sub-shower with longitudinal and transverse profiles parameterised as a function of altitude, energy and obliquity. In practice, the muon and electron/photon components of the transverse profile are treated separately. The application to electromagnetic showers (induced by decay photons of neutral pions) is presented in Section 2, and to hadronic showers in Section 3. Section 4 presents the details of the parameterisation procedure and illustrates the use of the code on a simple example.

1. INTRODUCTION, MOTIVATIONS

1.1 Ultra High Energy Cosmic Rays and the Pierre Auger Observatory

This work fits in the general framework of the association of VATLY, the Ha Noi cosmic ray laboratory where it has been performed, with the Pierre Auger Observatory. The present Section is an introduction to this Observatory and to the physics and astrophysics questions that it is addressing.

1.1.1 Generalities

Cosmic rays [1] are ionised nuclei that travel in space up to extremely high energies of the order of 10^{20} eV=16 Joules. There are very few of them but their contribution to the energy density of the Universe is similar to that of the Cosmic Microwave Background or of the visible light or of the magnetic fields, namely ~1 eV/cm^3. Their power law energy spectrum (Figure 1.1), spanning 32 decades (12 decades in energy), is of the approximate form $E^{-2.7}$.

The Pierre Auger Observatory [2] studies the high energy part of the spectrum, where an extra galactic component can be found. Its energy density is estimated to some 2 10^{-19} erg/cm^3 implying a power of ~10^{37} erg/Mpc^3/s. Both active galactic nuclei (AGN) and gamma ray bursts (GRB) stand, from the point of view of energy, as possible sources. One speaks of Ultra High Energy Cosmic Rays (UHECR) when the energy exceeds ~$10^{18.5}$ eV.

Three major questions are being addressed by such studies, with the aim of understanding the acceleration mechanism at play: Which is the energy distribution of UHECR's? Where do they come from? Which is their nature?

At lower energies, cosmic rays are found to be ionised nuclei with relative abundances similar to those measured in general in the
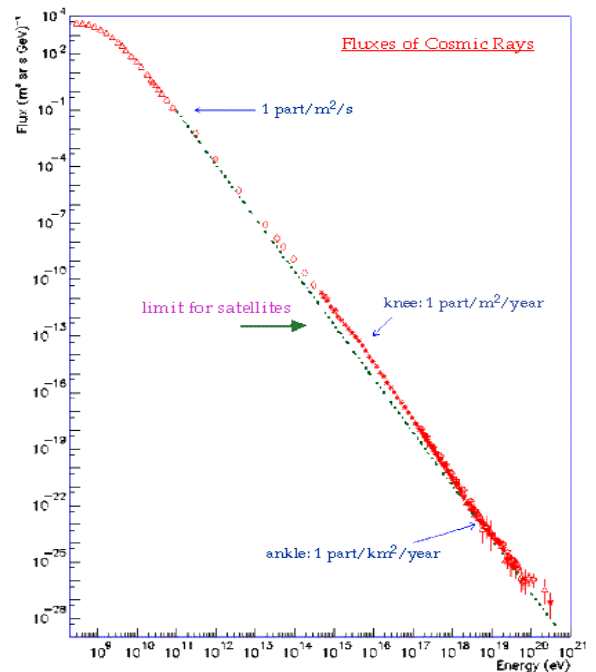

Figure 1.1: The cosmic ray energy spectrum displaying its main features.

Universe: protons dominate, followed by helium nuclei and by a spectrum of strongly bound light nuclei, mostly iron. Spallation reactions occurring in the interactions of cosmic rays with interstellar matter tend to fill the valleys of the original spectrum.

Most lower energy cosmic rays are galactic and have their sources in the shells of young Super Nova Remnants (SNR) in the Milky Way, the acceleration mechanism being well described by diffusive shock acceleration across the shock front [3]. This is a collisionless process, with magnetic fields causing the random walk progression of the particle being accelerated, implying many successive traversals of the shock front. Each shock traversal increases the particle energy by a constant fraction, proportional to the relative velocity of the upstream medium with respect to the downstream one. Turbulences around the shock result in strong magnetic field amplification increasing significantly the efficiency of the acceleration process. Diffusive shock acceleration has the property to generate a power energy spectrum with an index ~2 to 3. If the same mechanism were responsible for the acceleration of UHECR's, it would require much larger shocks, and possibly larger magnetic fields, than found in SNR shells.

The identification of SNR shells as sources was only made possible, in the case of galactic lower energy cosmic rays, by the availability of gamma ray telescope arrays, such as HESS in Namibia. What is detected is not the primordial cosmic ray but the decay photons of neutral pions produced in the interaction of the primordial cosmic ray with its environment. At UHECR energies, the rates are too low to use such a method. However, one may now hope to be able to identify counterparts directly, the energy being so high that bending in magnetic fields along the path from the source to the earth should no longer prevent such associations.

1.1.2 Extensive Atmospheric Showers and the Pierre Auger Observatory

The Pierre Auger Observatory (PAO) is a hybrid detector covering 3'000 km^2 where showers are detected from the fluorescence they produce in the atmosphere and by their impact on a ground detector array (Figure 1.2). Construction of the baseline design was completed in June 2008. With stable data taking starting in January 2004, the world's largest data set of osmic ray observations had been collected already during the construction phase of the Observatory.

When a primary cosmic ray enters the Earth atmosphere, it interacts with it and produces a large number of mesons, which, in turn, interact with the atmosphere, and so on until the primary energy is exhausted in ionisation losses. The result is a cascade of interactions (Figure 1.3) producing an extensive air shower (EAS). Its longitudinal profile evolves slowly with energy, in proportion to its logarithm, while its energy content, in the form of ionisation losses, is proportional to energy.
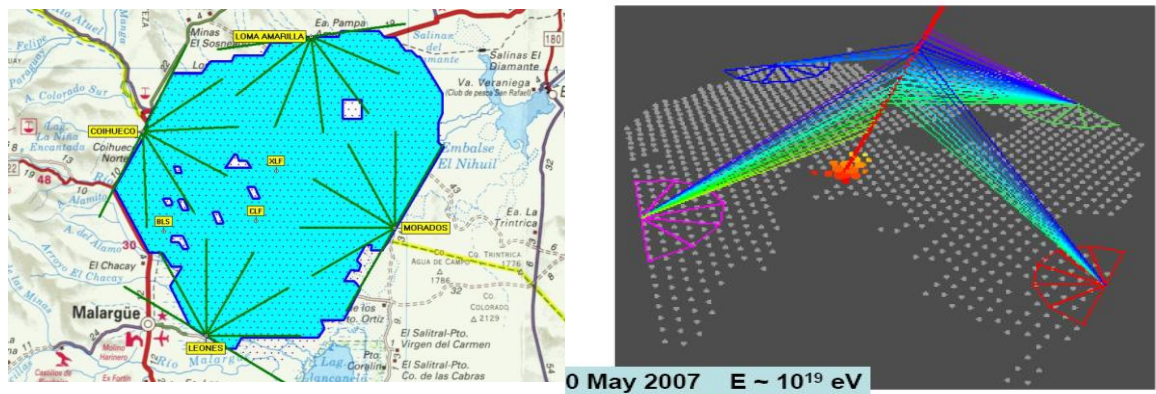

Figure 1.2 Left: Plan view of the PAO, covering some 60×50 km^2. SD tanks are shown as dots and the lines of sight of the 24 FD telescopes as green lines.
Right: The first four-fold hybrid event (when the array was not yet complete).

A major fraction of the mesons produced are pions, either neutral or charged. The former decay promptly into two photons and are therefore lost for the development of the hadronic cascade. They generate instead electromagnetic showers consisting mostly of electrons, positrons and photons, developing longitudinally at the scale of a radiation length, twice as short as the interaction length which governs the development of the hadronic cascade. The charged pions have a chance to decay into a muon-neutrino pair if their decay length, 56 m/GeV, is short enough in comparison with the interaction length. As a result, the muon to electron/photon ratio increases with depth.
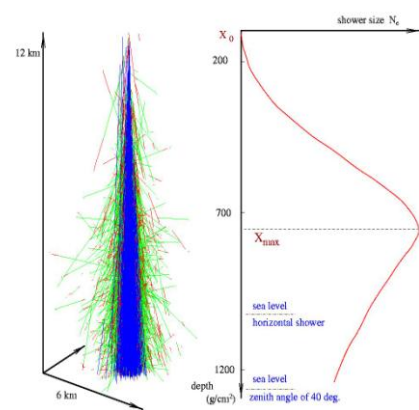

Figure 1.3: Development of an extensive air shower in the atmosphere.
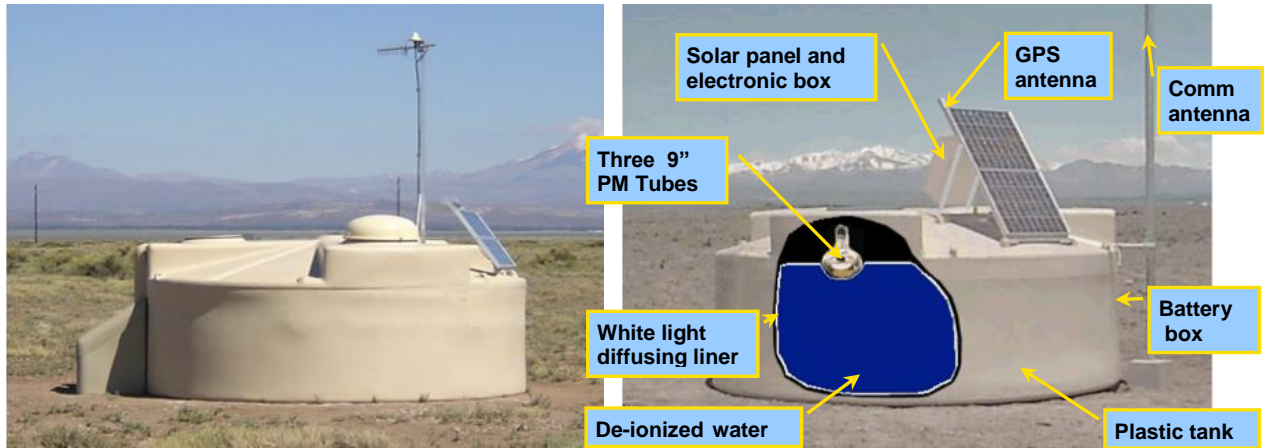
5

Figure 1.4: Picture of a Cherenkov tank on site (left panel) and exploded view (right panel).
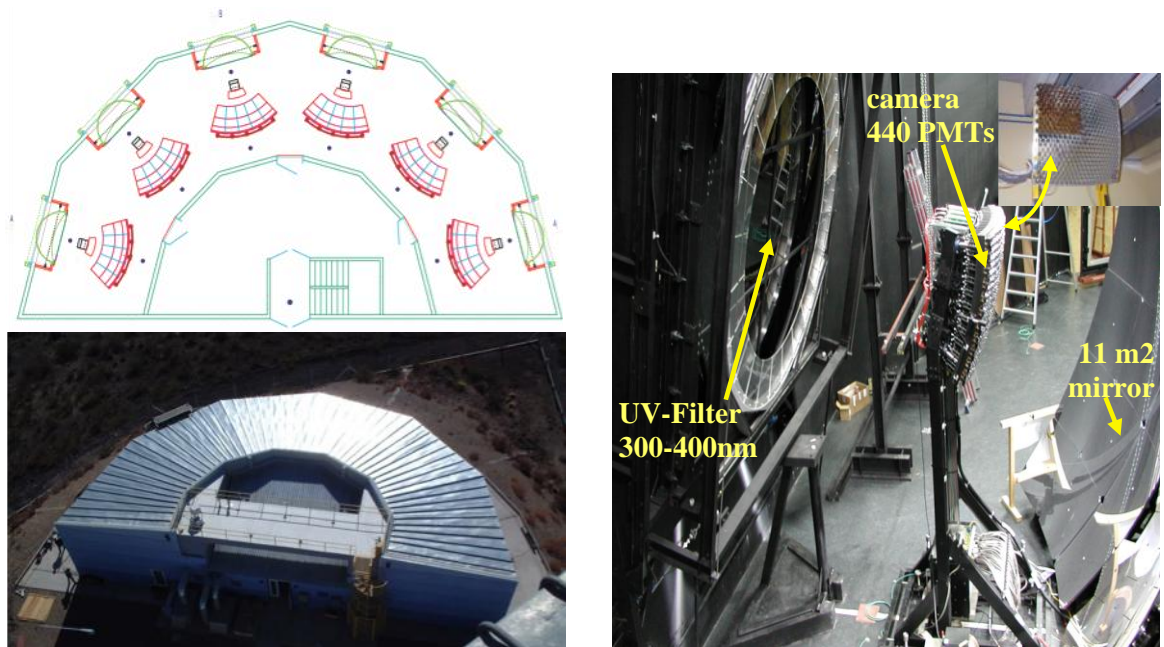
Figure 1.5 Left: A fluorescence station: schematic view (on top) and its photograph. Right: Picture of an eye.

Around 30 EeV, the UHECR flux is about $0.2 \, \text{km}^{-2}\text{century}^{-1}\text{sr}^{-1}\text{EeV}^{-1}$ and drops rapidly at higher energies, requiring a very large coverage, but the showers contain billions of particles when reaching ground and cover several square kilometres, allowing for a thin sampling. The PAO covers 3000 km^2 in the Argentinean pampas, of which only 5 ppm are covered by detectors. These include 1660 Cherenkov detectors making up the surface detector (SD, Figure 1.4), and 24 fluorescence telescopes making up the fluorescence detector (FD, Figure 1.5). Data are transferred by radio to an acquisition centre

which filters them and sends them out for subsequent dispatching to the laboratories associated with this research, including VATLY in Hanoi.

1.1.3 Data reduction

The FD is organized in four stations of six telescopes each, which overlook the PAO area. They measure the fluorescence light (near UV) produced in the interaction between the shower charged particles and the nitrogen molecules of the atmosphere. They can only operate during clear moonless nights, which implies a duty cycle of ~13%. Each telescope covers a field of view of 30° in azimuth and 28.6^o in elevation. After having been filtered, the light is reflected by a concave mirror onto an array of 440 hexagonal PMT pixels. In principle, a single telescope is sufficient to measure the direction of the shower axis from the measurement of the times at which each pixel is hit. But, in practice, a precise measurement requires either binocular detection or, less demanding, the simultaneous detection of the time at which at least one of the ground Cherenkov detectors has been hit by the shower. The energy is measured from the longitudinal profile which, when accurately and fully measured, provides a direct calorimetric evaluation of the shower energy (the energy carried away by neutrinos and muons penetrating ground is of the order of 10% and does not much fluctuate from shower to shower). However, in practice, this measurement is difficult: it implies a good knowledge of the air transparency and of the atmospheric Cherenkov light contamination and, most of the time, the shower is only partly contained in the field of view. Figure 1.6 illustrates the information available from the SD.

The SD samples the footprint of the showers on ground. It is made of a triangular array of water Cherenkov counters having a mesh size of 1.5 km deployed on flat ground at an altitude of 1400 meters above sea level, near the maximum of shower development for the highest energy vertical UHECRs. When reaching ground, showers consist essentially of low energy electrons, positrons and photons as well as of muons having a kinetic energy of a few GeV. The muon signal is proportional to track length while electrons and photons produce small showers at radiation length scale that are fully contained in the detector.

When shower particles are detected in at least three counters, the measurement of the time at which they are hit allows for a precise measurement of the azimuth and zenith angle of the shower axis accounting for the slight curvature of the shower front.

A FD event

Longitudinal shower profile with a fit to a Gaisser Hillas function.
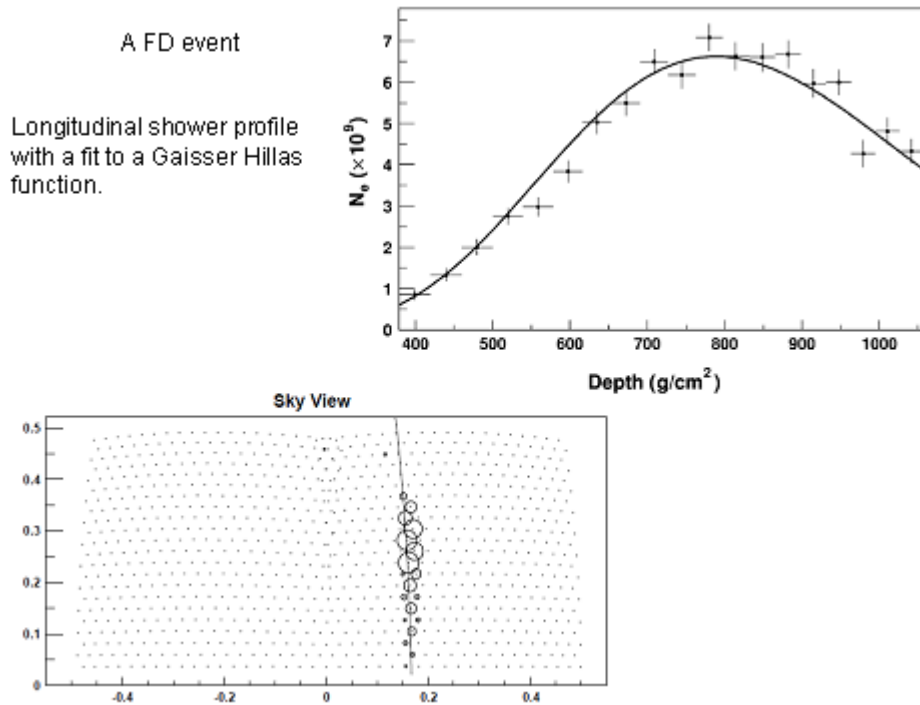
Sky View

Figure 1.6: A typical FD event showing the pixel pattern (bottom) and fit to the longitudinal profile (top).

The energy measurement is indirect but much easier than in the FD case. It implies the construction of a standard function, called lateral distribution function (LDF), which gives the average signal measured in a Cherenkov tank as a function of shower energy, distance to the shower axis and zenith angle. The zenith angle dependence is evaluated under the hypothesis of an isotropic cosmic ray flux. The energy is essentially measured by the normalization of the measured signals to the standard LDF at a distance of 1000 meters from the shower axis. The choice of such a reference is dictated by two scales: the tank spacing, 1.5 km, and the size of the shower detectable footprint on ground, which increases only slowly, logarithmically, with energy. In practice the influence of the former is dominant. The final energy scale is calibrated using FD data in hybrid events as illustrated in Figure 1.7. Figure 1.8 summarizes the information gathered by the SD, showing both the footprint of the shower on ground and the fit to the LDF.
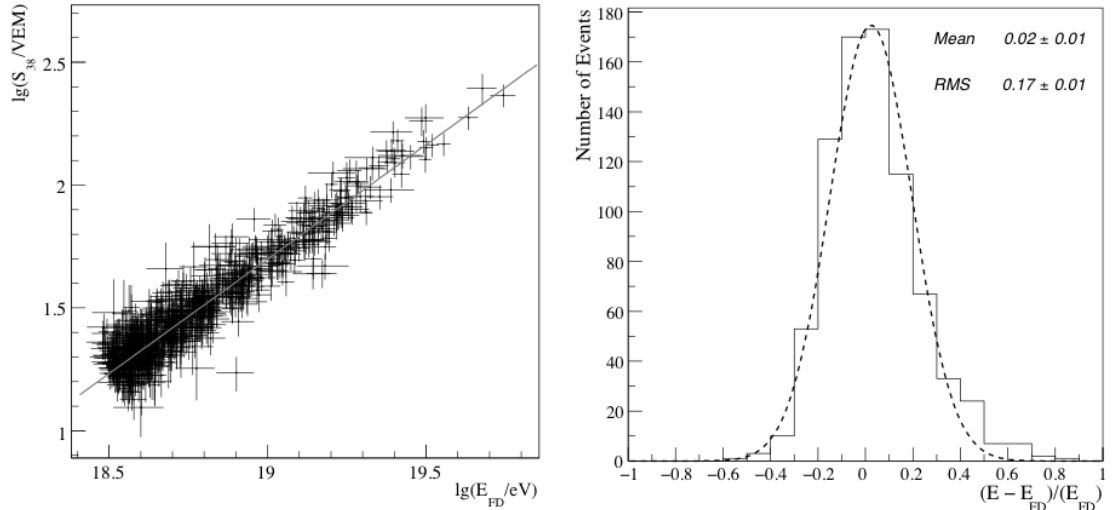
Figure 1.7: Hybrid events. Left: Correlation between the decimal logarithms of the energy measured in the FD (abscissa) and of the normalization (ordinate) of the measured SD signals to the value of *S(1000)*. Right: Fractional difference between the calorimetric energy, E_{FD}, and the energy estimate of the surface detector, E.
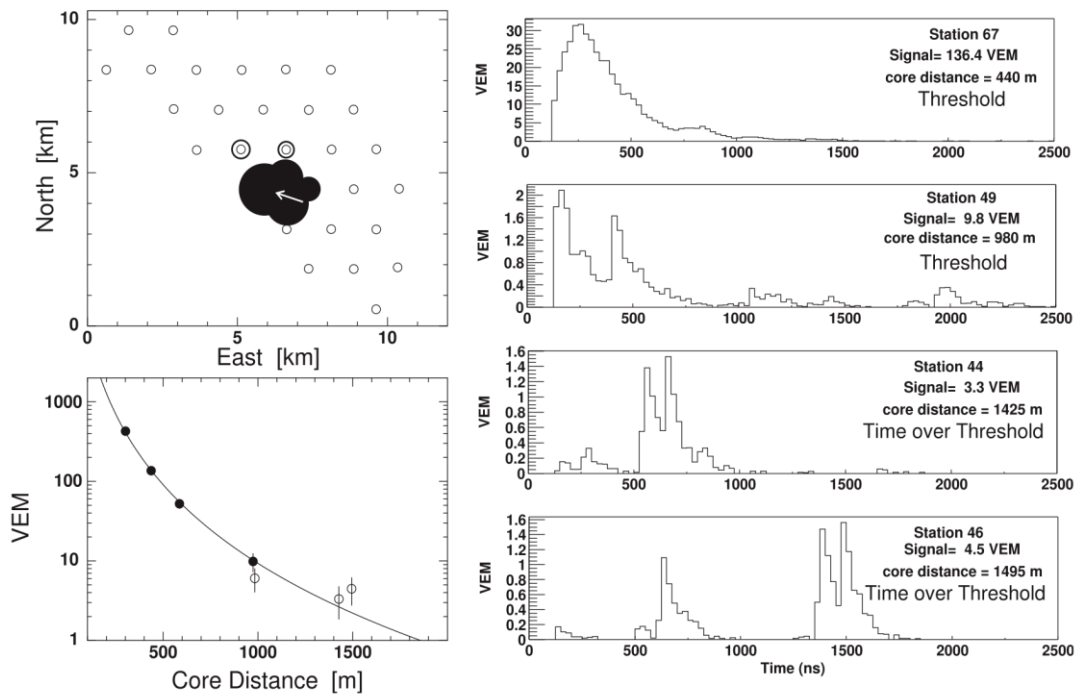
Figure 1.8: SD data of a typical event of about 5×10^{18} eV: Top left: Top view of triggered tanks. Lower left: LDF fit. Right: FADC traces from four detectors.

1.1.4 Some PAO important contributions

The PAO has already given two particularly important contributions to the physics of UHECRs. One is the evidence for the so-called GZK cut-off [4], the other is the observation of a correlation between the direction of arrival of the highest energy UHECR and nearby galaxies.

For some time, the differential spectral index of the energy spectrum has been known to change at ~ 3 10^{15}eV from 2.7 to 3.0 (the knee), and again back to 2.7 near the upper end of the spectrum (the ankle). The latter is often attributed to the transition from galactic to extra galactic sources, although some models accommodate extra galactic origins below the ankle. Sensible scenarios can be produced which reproduce the data. Of particular relevance to such scenarios are the interactions of cosmic rays with the cosmic microwave background (CMB), producing either electron-positron pairs or new mesons. Of these, the pion photoproduction threshold is of particular importance and causes the so-called Greisen-Zatsepin-Kuzmin (GZK) cut-off at the end of the spectrum, from the name of the physicists who first predicted the effect. Until recently, the existence of such a cut-off was uncertain but the Pierre Auger Observatory has given evidence for it. With a typical interaction length in the few 10 Mpc scale, cosmic rays coming from larger distances cannot make it to the Earth without interacting, and therefore loose energy: their flux is significantly damped and only nearby (<100 Mpc) sources can contribute to the UHECR spectrum.

The most recent PAO data, combining both SD and FD data, are illustrated in Figure 1.9 showing the fractional difference of the spectrum with respect to an assumed flux of spectral index 2.6. Two features are evident: an abrupt change in the spectral index near 4 EeV (the "ankle") and a more gradual suppression of the flux beyond about 30 EeV corresponding to the GZK cut-off.

The large UHECR statistics accessible to the PAO has revealed a correlation with extragalactic counterparts. Of relevance to this study is the fact that the nearby universe (100 Mpc radius), in which detected UHECRs are confined by the GZK cut-off, is highly inhomogeneous (Figure 1.10). Selecting UHECR having an energy in excess of 6 10^{19} eV and comparing the direction in the sky where they come from with a catalogue of nearby (<75 Mpc) galaxies, revealed a clear correlation (Figure 1.10). There was an even better correlation with nearby AGNs (of which, however, there

exists no complete catalogue). The correlation disappeared when including lower energy cosmic rays (pointing accuracy) or farther away galaxies (GZK cut-off).
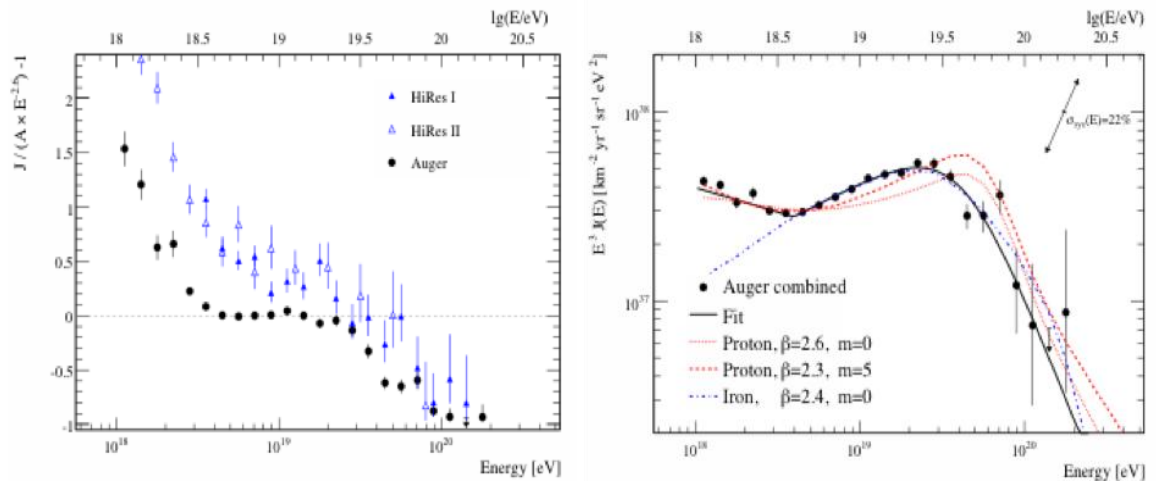
Figure 1.9 Left: Fractional difference between the combined energy spectrum of the PAO and a spectrum with an index of 2.6. Data from HiRes are shown for comparison. Right: Combined energy spectrum compared with several astrophysical models including a pure composition of protons (red lines) or iron (blue line).

An update of these data including data collected through 31st March, 2009 and corresponding to an exposure of 17040 km^2 sr yr ($\pm 3\%$), nearly twice the former value, brings in 31 additional events above the energy threshold of 55 EeV. The systematic uncertainty on energy is ~22% with a resolution of ~17% while the angular resolution of the arrival directions is better than 0.9^o. During the period reported earlier, 18 out of 27 events arrive within 3.1^o of an AGN in the VCV catalogue with red shift less than 0.018 while of the 31 additional events, only 8 have arrival directions within the prescribed area of the sky, not significantly more than the 6.5 events that are expected to arrive on average if the flux were isotropic: the degree of correlation with objects in the VCV catalogue has decreased with the accumulation of new data. Yet, possible biases have been carefully explored and discarded.

Figure 1.10: The nearby Universe

Figure 1.11: Circles of 3.1^o are drawn around 27 UHECR detected by the PAO up to year 2007; red crosses are 472 AGN (318 in field of view) having *z<0.018* (*D<75*Mpc). The solid line shows the field of view (zenith angle $< 60^o$) and the colour tells the exposure. The dashed line is the super galactic plane.

1.1.5 Identification of the primaries

Low energy cosmic rays are known to have abundances similar to those found in interstellar matter with a predominance of protons. At UHECR energies, however, the mass composition of primaries is uncertain. Measuring the mass distribution of the primaries in a range spanning essentially from protons to iron nuclei, higher mass nuclei being much less likely, is therefore a major challenge.

The main difference between showers induced by protons and by iron nuclei results from the very different natures of their first interaction in the upper atmosphere. The proton shower starts to develop on average after having crossed one interaction length and the depth of its starting point fluctuates with a variance also equal to one interaction length. The iron shower, in an oversimplified picture, may be seen as the superposition of 56 proton showers (protons and neutrons are equivalent at such energies), each carrying 1/56 of the nucleus energy. As a result it starts much earlier, and the location of its starting point fluctuates much less, than in the proton case. From then on proton and iron showers develop in the same way. While such a description is useful to provide a simple qualitative explanation of what is going on, the reality is far more complex and its details are not well understood. Not all nucleons of the colliding nuclei interact the same way. In a simplified picture, some nucleons − one refers to them as wounded nucleons − interact as if they were independent nucleons while the other nucleons − one refers to them as spectator nucleons − are unaffected. This, again, is an oversimplified view of reality. Glauber model [5] provides a recipe to evaluate the number of wounded nucleons.

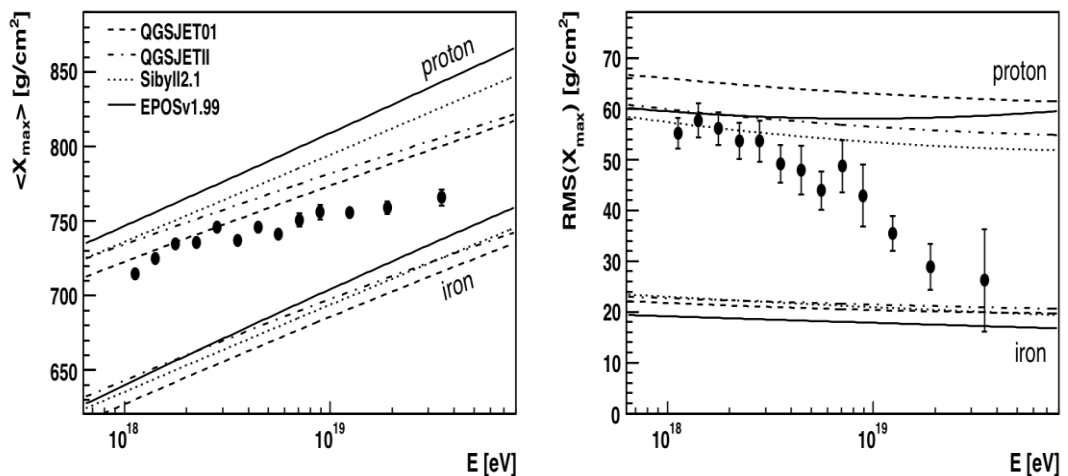Figure 1.12: $<X_{max}>$ and $RMS(X_{max})$ compared with air shower simulations using different hadronic interaction models.

Nevertheless, as a general rule, in order to distinguish between light and heavy incident nuclei one will aim at measuring quantities that are sensitive to the early shower development. These include, among others, the longitudinal profile, the rise time and the muon abundance. The FD is

used to measure with good resolution the shower longitudinal profile and the depth at which the shower reaches its maximum (X_{max}). At a given energy, the mean and the width of the X_{max} distribution are both correlated with the cosmic ray mass composition. Proton showers penetrate deeper into the atmosphere (larger values of X_{max}) and have wider X_{max} distributions than heavier nuclei. In practice, however, such a measurement is difficult and a strict selection of useful events is mandatory. The most recent PAO results are shown in Figure 1.12 together with predictions of popular hadronic models for both protons and iron nuclei.

The time profile of particles reaching ground is sensitive to the shower development as the first portion of the signal is supposed to be dominated by muons which arrive earlier and over a period of time shorter than electrons and photons. A rise time ($t_{1/2}$) is defined for each tank FADC trace as the time to go from 10% to 50% of the total integrated signal. To the extent that both rise time and X_{max} are expected to be sensitive to the primary mass composition, they should display a clear correlation. Evidence for it is obtained by unfolding the dependence of the rise time on zenith angle and distance to the shower axis. This is done by defining a standard function, in the same spirit as was done for the LDF, and using a particular energy (10^{19}eV) as reference − as one uses the particular distance of 1000 meters for *S(1000)*. The resulting quantity, called Δ_i, increases on average with energy as expected for showers developing deeper into atmosphere (Figure 1.13 left) and is indeed clearly correlated with X_{max} as shown in Figure 1.13 right.

Another property displayed by the rise time is its dependence on tank azimuth ζ measured around the shower axis, the more so the more inclined is the shower. When an inclined shower reaches ground, the upstream tanks are hit first and the downstream tanks are hit last. The former probe the shower at an earlier stage of development than the latter do. But there is also a pure geometric effect that differentiates between upstream and downstream tanks. The path length for particles to reach an upstream tank from the shower axis is much shorter than that to reach a downstream tank with the result that the former are seen under a larger solid angle than the latter and therefore detect a larger signal.
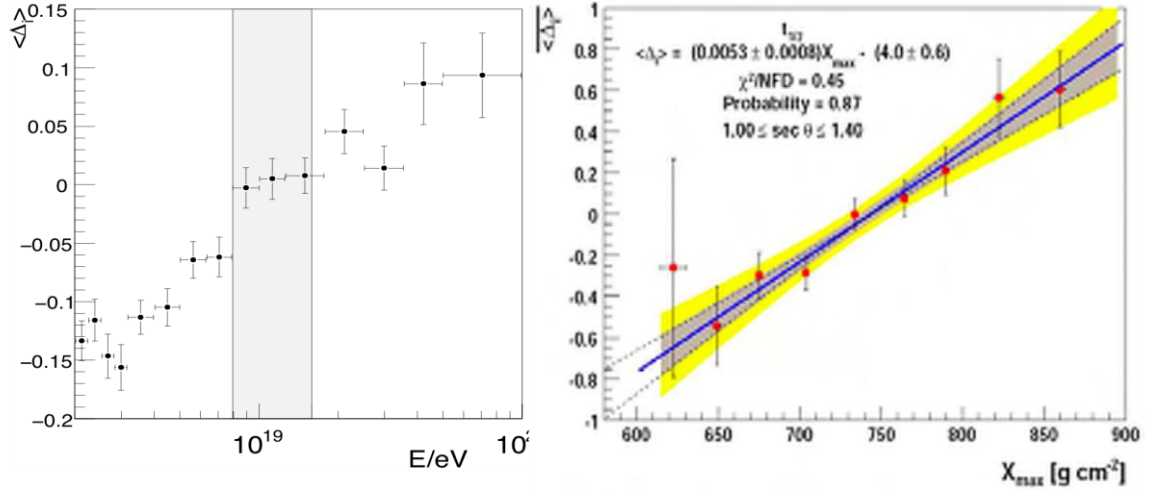
Figure 1.13 Left: SD events; dependence of the mean value of Δ_i on energy. Right: Hybrid events; dependence of the mean value of Δ_i on X_{max}. A correlation is found which is parameterised with a linear fit. The shaded areas show the estimated uncertainty (one and two σ), obtained by fluctuating each point randomly within the measured error bar and repeating the fitting procedure.

Moreover, as noted earlier, the mean response to muons − most muons having sufficient energy to feed through the tanks − is independent, on average, from the angle of incidence. On the contrary that of electrons and photons − generating small showers in water − depends on the angle of incidence in the same way as does the tank section normal to the incoming particle momenta. The net effect is an azimuthal asymmetry of the tank responses around the shower axis, trivially increasing with the distance r of the tank to this axis. This asymmetry is in particular visible on the azimuthal dependence of the rise time and is observed to reach a maximum around 50° zenith angle independently from energy. Interpreting this result in terms of mass composition implies that the mean primary masses increase with energy, a result consistent with the FD measurements of the longitudinal profile, suggesting a transition from proton dominance − light nuclei − to iron dominance − heavier nuclei − when the energy increases from 1 to 30 EeV.

1.1.6 Muon abundance

An indicator of the shower age is the relative muon abundance, which increases with age: at a same depth, iron showers are therefore expected to be more muon-rich than proton showers are. While no direct measurement of the muon abundance has yet been made, numerous attempts at measuring quantities closely related to the muon abundance

have been explored. Such is the rise time, which was presented in the preceding section.

Other approaches include attempts at identifying muons from sudden jumps in the FADC traces (the "jump method") and a direct evaluation of the muon signal by subtraction of the electron-photon contribution from the FADC trace.

This latter method implies that the electron-photon signal (i.e. the contribution given by electrons and photons to the FADC traces) is a function of energy, zenith angle and depth (measured with respect to X_{max}) having a zenith angle dependence obtained from the hypothesis that the bulk of detected showers are isotropic and an energy dependence known from hadron models. Under such assumptions, the muon abundance is the only unknown. When measured relative to that predicted for proton primaries, it is 1.53+0.08 (stat.)+0.21 (syst.). Pure iron composition would predict a lower factor, of the order of 1.3.
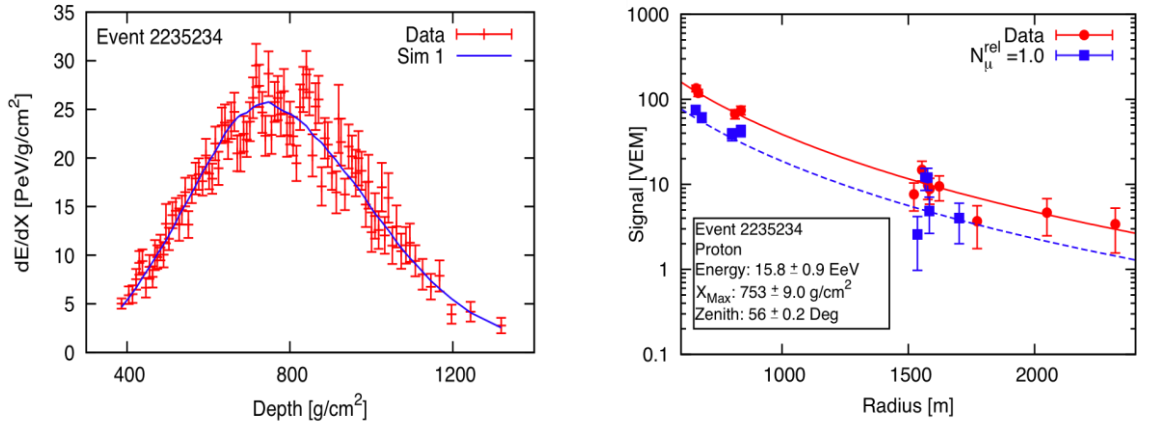
Figure 1.14: Measured longitudinal (left panel) and lateral (right panel) profiles for one of the hybrid events. The best-matching simulation is shown as squares and dashed line in the lateral distribution while the measured SD signal (circles, full lines) is more than twice as large.

Additional evidence is obtained by the analysis of hybrid events where the longitudinal profile is used to choose between a proton and an iron hypothesis, whatever is best, and to then predict the amplitude of the signal on ground (Figure 1.14). A similar conclusion is also reached from analyses of the FADC traces such as done with the jump method: the muon abundance inferred from such analyses is significantly larger than that predicted for iron by popular hadronic models. Figures 1.15 and 1.16

summarize the results. A possible interpretation is to dispose of the problem by blaming it on a 30% underestimate of the FD energy scale, as illustrated in Figure 1.16. However, an energy independent analysis [6] rather suggests that the hadronic models used in the simulation predict too steep a muon lateral distribution function. This is indeed another way to increase the amplitude of the muon component in the D range explored by the SD. Moreover it would explain why the azimuthal asymmetry of the rise time gives results in agreement with the FD X_{max} measurement, as both probe the longitudinal profile independently from the lateral distribution function.
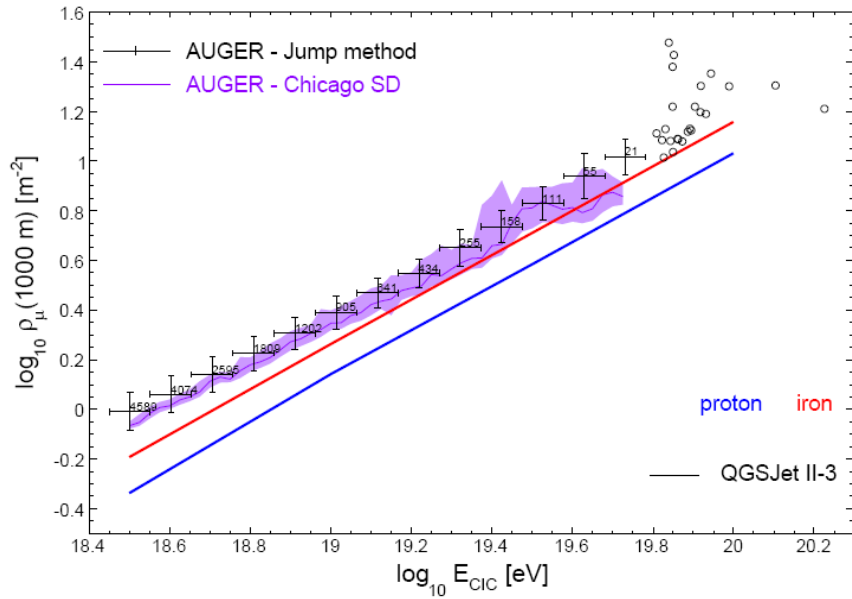
Figure 1.15: Results of earlier studies on primary composition.

In summary, the mass composition of UHECR primaries remains an open question. Major progress has been achieved in the analysis of FD data where a rigorous treatment of possible biases and systematic uncertainties is now available. The results are consistent with the predictions of hadronic models and, in such a picture, provide evidence for a transition from proton-like to iron-like primaries over the energy range covered by the PAO, say 1EeV to 30 EeV where the GZK threshold becomes effective. This conclusion is also reached, with lesser accuracy, by the analysis of the azimuthal rise time asymmetry in the SD, an analysis sensitive to the depth at which the longitudinal shower profile starts declining. Yet, SD analyses that are sensitive to the amplitude of the muon signal can only be made consistent (barely) with the predictions of hadronic models at the price of a 30% increase of the energy scale. A possible cause might be the

inadequacy of hadronic models to reproduce the lateral distribution function of muons. Another possible cause might be the inadequacy of the detector simulation to describe the response to muons. However, in spite of numerous attempts, no evidence has ever been found that such might be the case.
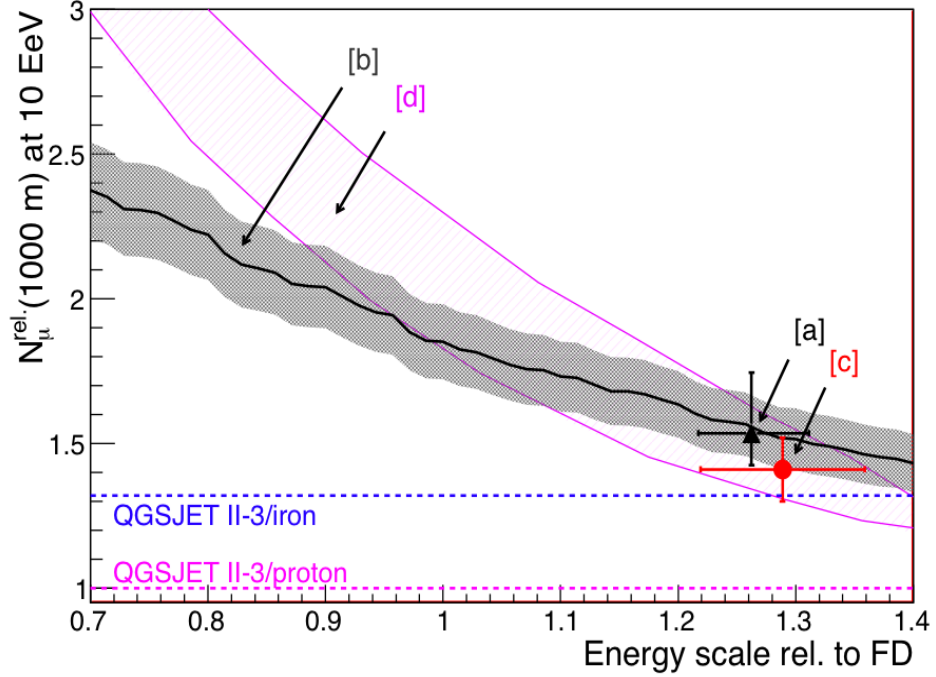
Figure 1.16: Number of muons at 1000 m relative to QGSJET-II/proton vs. the energy scale from different SD analyses (see text). The events have been selected for $\log_{10}(E/eV)$ = 19.0 ± 0.02 and $\theta \le 50^{\circ}$. According to the tested model, iron primaries give a number of muons 1.32 times bigger than that from protons (horizontal lines in the figure).

1.2 Simulations

1.2.1 Generalities

As amply illustrated by the preceding sections, the analysis and interpretation of cosmic ray data is complicated by the impossibility to access directly primaries: all measurements are made on secondaries, components of the showers induced by the interaction of the primaries with the atmosphere.

To obtain information on the primaries, a model of these interactions and of the development of extensive air showers in necessary. The performance of such a model and the quality of the simulations that it offers are essential factors of success in the analysis and interpretation of cosmic ray data.

Such simulations imply the ability to describe precisely both the shower development and the detector response. To the extent that the physics of fluorescence and Cherenkov radiations are well known and understood, the latter is in principle straightforward but, in practice, quite complex. Simulating the FD data implies a good knowledge of the transparency of the atmosphere, including its aerosol content, and a good evaluation of the main backgrounds, including Cherenkov light radiated in the atmosphere. Simulating the SD data requires a detailed understanding of the Cherenkov detectors, including a good knowledge of the water transparency and liner diffusivity as a function of wave length, of the quantum efficiency of the photocathode, again as a function of wave length, of the collection efficiencies at the first and second dynodes as a function of photon impact, of the PMT gains, of the electronic and thermal noises, of the after-pulsing characteristics, etc. Much effort has been dedicated in the PAO collaboration to produce computer codes that offer adequate descriptions of the SD and FD responses.

The former, however, namely the simulation of the shower development proper, addresses an energy and rapidity range in which the characteristics of the hadronic interactions of nuclei, baryons and mesons with air are unknown. One needs to rely on hypotheses, some of which are highly conjectural. Indeed, most of our knowledge of very high energy hadronic interactions has been obtained from proton-antiproton collisions and is now being upgraded with LHC data becoming available. In addition to this fundamental problem, a technical difficulty results from the very large number of shower particles, which precludes following each of them individually in a Monte Carlo code. In order to cope with the need to keep computer time within reasonable limits, various techniques have been developed, none of which, however, is fully satisfactory.

General programs are available to simulate extensive air showers. In particular, CORSIKA and AIRES offer general frames that can accommodate a number of hadronic interaction models. They have been used by the PAO Collaboration to generate a library of proton and iron showers covering the energy range from 10^{17} to 10^{20} eV and a range of zenith angles between 0° and 70°. However, such codes are often seen as black boxes and lack flexibility.

1.2.2 Main difficulties and present approach

Our knowledge of high energy hadronic interactions has its source in experiments performed on four major colliders: proton-antiproton colliders at CERN and Fermilab (Tevatron) reaching 1+1=2 TeV in the cms, corresponding to $2 \cdot 10^{15}$ eV for cosmic rays; LHC at CERN reaching 3.5+3.5=7 TeV in the cms, corresponding to $2.5 \cdot 10^{16}$ eV for cosmic rays; heavy ion colliders at RHIC (Brookhaven, Au, 100 GeV/nucleon) and LHC (CERN, Pb, 1.38 TeV/nucleon). To reach the UHECR regime implies an extrapolation by nearly four orders of magnitude.

Moreover, the region of phase space explored by such colliders is different from the region of relevance to the development of extensive air showers. The former is the central, the latter the forward rapidity region. The forward rapidity region is confined to the beam pipe in collider experiments, three units of rapidity correspond to less than 6°.

In cosmic ray interactions, the target is always a nucleus, mostly nitrogen. There exist no collider data of hadronic interactions on nuclei in the proper energy and rapidity ranges.

In the development of extensive air showers, the projectile is usually a meson, mostly pions and kaons. There exist no collider data of hadronic interactions of mesons in the proper energy and rapidity ranges.

It is only because we believe to understand sufficiently well the strong interaction that we hope to be able to extrapolate available data into a region so dramatically unexplored by available collider data. We shall present the arguments of relevance in Section 3. Yet, this understanding is only in very general terms, no model can be considered reliable when it comes to details. Particularly crude is our understanding of nuclear interactions at such high energies and of how to relate them to nucleon-nucleon interactions.

Another major difficulty, which simulations have to face, is the prohibitive computing time required to follow in its totality the development of a shower. Sampling methods (thinning) are being used to cope with this problem but are not fully satisfactory (difficult handling of statistics and insufficient efficiency in computing time reduction).

The idea of the present work is to make available a simulation allowing for the rapid production of large quantities of ultra high energy showers. Such simulation must be flexible enough to allow for changing

the values of the parameters that govern the behaviour of hadronic interactions at ultra high energies. This gain in computer time, in flexibility and in transparency has a price: one can no longer pretend to construct a precise model having the ability to describe the interaction in all its details. Such an approach is somehow orthogonal to that taken by the standard simulation codes in use in the cosmic ray community.

The method used here consists in following the development of the sub-shower induced by a secondary only when its energy exceeds some predefined threshold. When it does not, one uses instead a parameterised description of the sub-shower, which makes it unnecessary to follow the details of its subsequent development. There are several arguments in favour of such an approach, which treats precisely and reliably the first interactions taking place in the development of the shower: the fluctuations observed in the development of showers induced by primaries of a same nature and of a same energy are dominated by the very first interactions; the difference between the developments of shower induced by primaries of different natures, say iron or proton, are governed by what happens at the first interaction; the lack of availability of adequate collider data affects only the higher energies. We shall return to this point in Section 3.

1.2.3 Electromagnetic and hadronic showers

The method just sketched has been applied successfully to the longitudinal development of electromagnetic showers, in particular to the study of ultra high energy phenomena such as the LPM (Landau-Pomeranchuk-Migdal) and Perkins effects [6,7]. Two features make such studies particularly simple. First, to an excellent approximation, the only possible shower constituents are electrons, positrons and photons and their interactions with matter reduce to pair creation in the case of photons and to bremsstrahlung in the case of electrons and positrons. Second, the shower development depends on a single scale, the depth inside the atmosphere, measured in radiation lengths. Section 2 gives a summary of the results and expands the simulation to the description of the transverse shower development.

At variance with the preceding situation, the development of hadronic showers is complicated by several factors:

– The description of the muon component, considered as an important element of the simulation, implies dealing with hadron decays; this introduces a new scale, the decay length, which is proportional to energy. The ratio between decay length and interaction or radiation lengths becomes therefore dependent on both energy and altitude. This is a major complication: the beauty of the single scale description applicable to electromagnetic showers is now lost.

– Many different hadrons are in principle being produced; the present study ignores this complication and assumes all secondaries to be pions.

– Hadronic interactions are dominated by meson-nucleus interactions, essentially pion-nitrogen interactions, of which, essentially, nothing is known in the energy domain of relevance. The description of high energy hadronic interactions is therefore inferred from what is known of proton-proton (or proton-antiproton) interactions. Sensible extrapolations need to be devised.

Section 3 expands on such considerations and describes how we deal with hadronic interactions. Section 4 describes the parameterisations used in the simulation. Section 5 gives some results.

2. ELECTROMAGNETIC SHOWERS

The longitudinal development of electromagnetic showers has been extensively studied in earlier work [8] with particular emphasis on the description of the Landau-Pomeranchuk-Migdal [9] and Perkins [10] effects. Both effects are essentially irrelevant to the present work and are ignored. Section 2.1 below summarizes the main results. However, the description of the transverse development was ignored in such earlier work. As it is an essential component of the lateral distribution function of UHECR showers, it needs to be taken in due account in the present simulation. Its treatment is described in Section 2.2.

2.1 Longitudinal shower development

The present work uses a simple model of the longitudinal development of electron and photon showers, retaining only pair creation and bremsstrahlung as relevant elementary processes. At very high energies, showers contain so many particles that it is impracticable to follow each of them in a simulation. Most existing codes deal with this problem by using statistical approximations, such as thinning [11]. The approach used here is different: as soon as a shower particle, electron or photon, has energy lower than some threshold, it is replaced by a parameterised sub-shower profile, considerably reducing the complexity of the problem. All what needs to be done is then to devise a proper parameterisation of the shower profile and to calculate the dependence on energy of the parameters. In practice, the mean and rms values of the parameters are calculated once for all as a function of energy and the sub-showers are generated accordingly with random Gaussian fluctuations of the parameters having the proper means and variances.

2.1.1 Elementary processes

Showers may be initiated by an electron (or positron, here electron is to be understood as electron or positron) or a photon and any other particle that may be created in the cascade (such as $\mu^+\mu^-$ pairs from photon conversion) is ignored. Moreover the only processes considered are pair creation in the case of photons and bremsstrahlung in the case of electrons, implying that Compton scattering, photoelectric effect, and other processes that are important at lower energies are not taken into account.

To a very good approximation, the probability d^2P for a photon of energy E to convert in a medium of radiation length X_0 over a thickness $dx=X_0dt$ (t has no dimension, dx and X_0 are measured in g/cm^2), into a pair having an electron of energy E in the interval $[\eta, \eta+d\eta]$ (the positron energy being in the interval $[E–\eta, E–\eta–d\eta]$) is

$$d^2P=\{1- 4/3\ \eta/E\ (1–\eta/E)\}d\eta/E\ dt \qquad (2.1)$$

The radiation length in air is 36 g/cm^2.

The dependence of $Ed^2P/d\eta dt$ on η/E is displayed in Figure 2.1 (left). It has a parabolic shape with a minimum of $2/3$ corresponding to the symmetric case (electron and positron having equal energies). It is symmetric in the exchange of the electron and positron (η/E becoming $1–\eta/E$). Integration over η/E gives $dP/dt=7/9$: the photon distribution over the thickness traversed, $x=tX_0$, is an exponential of the form $exp(–7/9t)$.

In the case of an incident electron of energy E, the probability d^2P to radiate, over a distance $dx=X_0dt$, a photon having an energy in the interval $[\eta, \eta+d\eta]$ is, to a good approximation,

$$d^2P= \{4/3- 4/3\ \eta/E + (\eta/E)^2\}\ d\eta/\eta\ dt \qquad (2.2)$$

It is illustrated in Figure 2.1 (right) where $d^2P/(dt\ d\eta/\eta)$ is shown against η/E. It reaches a minimum of $8/9$ at $\eta/E =2/3$ while being unity when $\eta=E$ and being 4/3 when $\eta=0$. The total energy bremsstrahled per interval dt is

$$\int\eta\ d^2P = \{4/3\ E- 4/3\ E/2 + E/3\}\ dt = E\ dt. \qquad (2.3)$$

The remaining energy has therefore an exponential dependence over the thickness $x=tX_0$ traversed of the form e^{-t}. However, the number of photons bremsstrahled is infinite, an infinite number of zero energy photons being radiated. Introducing a cut-off ε, the number of radiated photons having energy in excess of ε is obtained by integration over η between ε and E:

$$dN=\{4/3lnE/\varepsilon -5/6+ 4/3\ \varepsilon/E -1/2\ (\varepsilon/E)^2\}dt \qquad (2.4)$$

The multiplication of particles in the cascade is counteracted by the energy losses which they suffer. The critical energy, E_c, is defined as the energy where an electron looses as much energy by ionisation as it does by radiation. It is equal to 80 MeV in air. The strategy adopted here is to consider bremsstrahlung explicitly only for photons having an energy in excess of E_c, namely setting $\varepsilon=E_c$ in Relation 2.4. At $E=10^{21}eV$ with

$\varepsilon=E_c=80MeV$ and $dx=0.01X_0$, Relation 2.4 gives $dN\sim\{20-ln80-5/6\}0.01\sim$ *0.15*. Multiple photon radiation can therefore be safely neglected when using such small steps of *0.01* radiation lengths.

The energy radiated in the form of photons of energy lower than E_c is, in such a step:

$$dE=0.01\{4(E_c/E)/3-2(E_c/E)^2/3+(E_c/E)^3/3)E\} \tag{2.5}$$

The electron energy loss is calculated in each slice $dx=0.01X_0$ as the sum of the latter and of the ionization loss:

$$dE/dx=0.01E_c(1+0.15log_{10}[E/E_c])dt \tag{2.6}$$

In addition any particle, electron or photon, having energy lower than *1.5 MeV* is made to stop and to deposit its energy in the shower. Both this energy and the energy loss calculated using Relation 2.6 are deposited over two radiation lengths with a profile having a maximum at one radiation length.

The model has been checked against the result of a detailed simulation [12] for 30 GeV electrons in iron ($E_c= 20\ MeV$). The result is displayed in Figure 2.2 and shows quite good agreement given the high energy approximation used here.
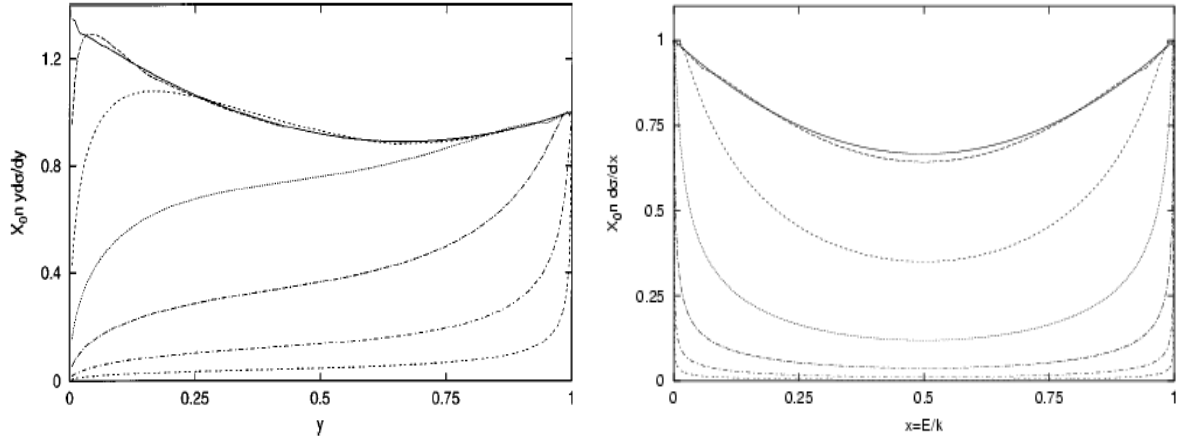

Figure 2.1 Left: Differential bremsstrahlung probability per unit of radiation length and per $d\eta/\eta$ as a function of the fractional energy taken away by the photon.
Right: Differential pair creation probability per unit of radiation length as a function of the fractional energy taken by the electron.
Full lines are without and dashed lines with LPM reduction.
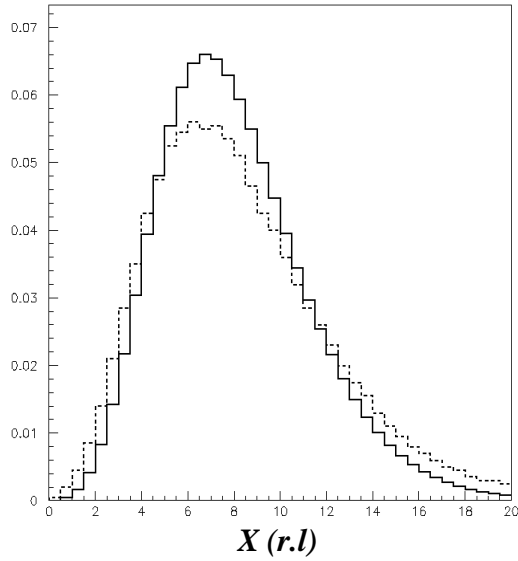
Figure 2.2: Average longitudinal profile of a shower induced by a 30 GeV electron in iron: full line, result of the present simulation; dotted line: EGS4 result [12].

2.1.2 Parameterisation of the profile

The form used here to parameterise the longitudinal shower profile is the standard Gaisser Hillas function [13].

$$S = S_{max}\{[X - X^*]/[X_{\max} - X^*]\}^{[X\max - X^*]/w} exp([X_{max} - X]/w) \qquad (2.7)$$

where S is the density of charged particles at depth X in the medium. In practice, SdX may be the sum of the charged particle track lengths in the transverse shower slice between X and $X+dX$, or the energy ionisation loss in that same slice, or even the amount of Cherenkov light produced in that same slice. At high energies, all three distributions are expected to have very similar shapes. The depth variable X is measured in g/cm^2 with dX being the product of the local density by the thickness of the slice. In atmospheric air the dependence of density on altitude distorts X with respect to actual distances.

The quantity X^* defines where the shower, understood as its charged particle components, starts developing. In the case of a photon, it starts at the location of the first pair creation while in the case of an electron it starts at $X^*=0$. Obviously, once started, the shower develops independently from X^* and S depends explicitly on $X–X^*$. It is therefore sufficient to consider showers induced by electrons, *i.e.* having $X^*=0$.

Taking S_{max} and X_{max} as units, one defines reduced variables $\eta=S/S_{max}$ and $\xi=X/X_{max}$. The reduced profile then reads $\eta=\{\xi exp(1-\xi)\}^\delta$ and depends on a single parameter $\delta=X_{max}/w$. Equivalently, $ln\eta=\delta(ln\xi+1-\xi)$.
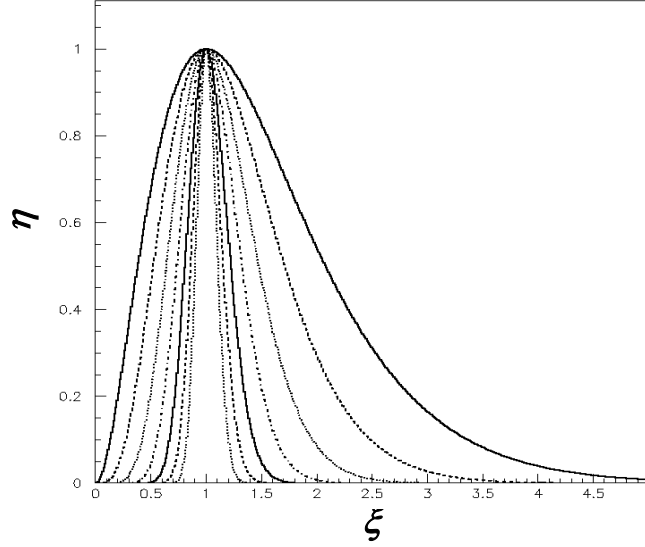
Figure 2.3: Reduced profiles for different values of δ (2, 4, 8, 16, 32, 64 and 256).

The reduced profile starts at *0* at origin as ξ^δ and approaches *0* again when $\xi\rightarrow\infty$. Differentiating gives $d\eta/d\xi=\eta\delta(1/\xi-1)$ which cancels for $\xi=1$ where η reaches its maximum value, *1*, independently from δ. Therefore, the real profile reaches its maximum value S_{max} at $X=X_{max}$ which justifies their names. The second derivative, $d^2\eta/d\xi^2=\eta\delta^2(1/\xi-1)^2-\eta\delta/\xi^2$ cancels for $\delta(1/\xi-1)^2=1/\xi^2$ or $\xi=1\pm1/\sqrt\delta$. While the turning points are equidistant from $\xi=1$ the profile is not at all symmetric around this value. As illustrated in Figure 2.3 it is significantly skewed, the more the larger δ. As $\delta>1$, the profile starts tangent to the ξ axis. Analytic expressions of the mean, rms and integral values are given in Table 2.1 below, both for the reduced profile and the real one.

The knowledge of $<X>$ and of $Rms(X)$ fixes w and X_{max}. The knowledge of $\Sigma=\int SdX$ then fixes S_{max}. Explicitly,

$$\delta = \{<X>/ Rms(X)\}^2 - 1 \quad X_{max} = <X>\delta/(\delta+1)$$

$$S_{max} = \Sigma\,\delta^{\delta+1}exp(-\delta)/\Gamma(\delta+1)/ X_{max} \qquad w = X_{max}/\delta$$

(2.8)

It has been checked that $<X>$ and $\rho=Rms(X)/<X>$ are not significantly correlated, thereby making it legitimate to apply independent Gaussian fluctuations to each.

Table 2.1. Gaisser Hillas parameters for an electron ($X^*=0$).

Parameter	Reduced profile	Real profile
Mean value	$1+1/\delta$	$X_0+X_{max}(1+w/X_{max})$
Rms value	$(\sqrt{1+\delta})/\delta$	$\sqrt{(w+X_{max})w}$
Integral	$J(\delta)=e^\delta\Gamma(\delta+1)/\delta^{\delta+1}$	$S_{max}X_{max}J(X_{max}/W)$

The dependence on energy of the mean and rms values of $<X>$ and ρ evaluated by the present simulation is illustrated in Figure 2.4. The parameters were calculated with full shower development up to an initial energy of *100 GeV*. Above this energy, any shower particle having an energy smaller than *40%* of the initial energy was replaced by a Gaisser Hillas profile evaluated for the proper values of the relevant parameters (after application of Gaussian fluctuations). The start of the profile was defined as $X^*=0$ for electrons and was chosen at random with an $exp(-[7/9]X^*/X_0)$ distribution for photons. As $E_c=80\ MeV$ is the only scale of the problem, the development of the profile scales in proportion with the logarithm of the energy as soon as E_c is negligible with respect to initial energy.

Because of shower to shower fluctuations, the parameters that describe the average profile (obtained as superposition of a large number of different showers) are not exactly the same as the mean values of the parameters that describe individual profiles (as displayed in Figure 2.4). More precisely, the mean value of the former profile, $<X'>$, and that of the mean values of the latter profiles, $<<X>>$, are equal and can be parameterized as *3.22+2.34log₁₀E*. But the ρ parameter of the former profile, ρ', and the mean value of the ρ parameters of the latter profile, $<\rho>$, differ. In the case of the latter profiles, the rms values of the quantities $<X>$ and ρ define the size of the shower to shower fluctuations. To a very good approximation, *Rms(<X>)* is constant and equal to *0.94±0.01* radiation lengths. On the contrary, *Rms(ρ)* is found to decrease with energy as $Rms(\rho)=0.001+16.20/(log_{10}E+5.6)^3$.
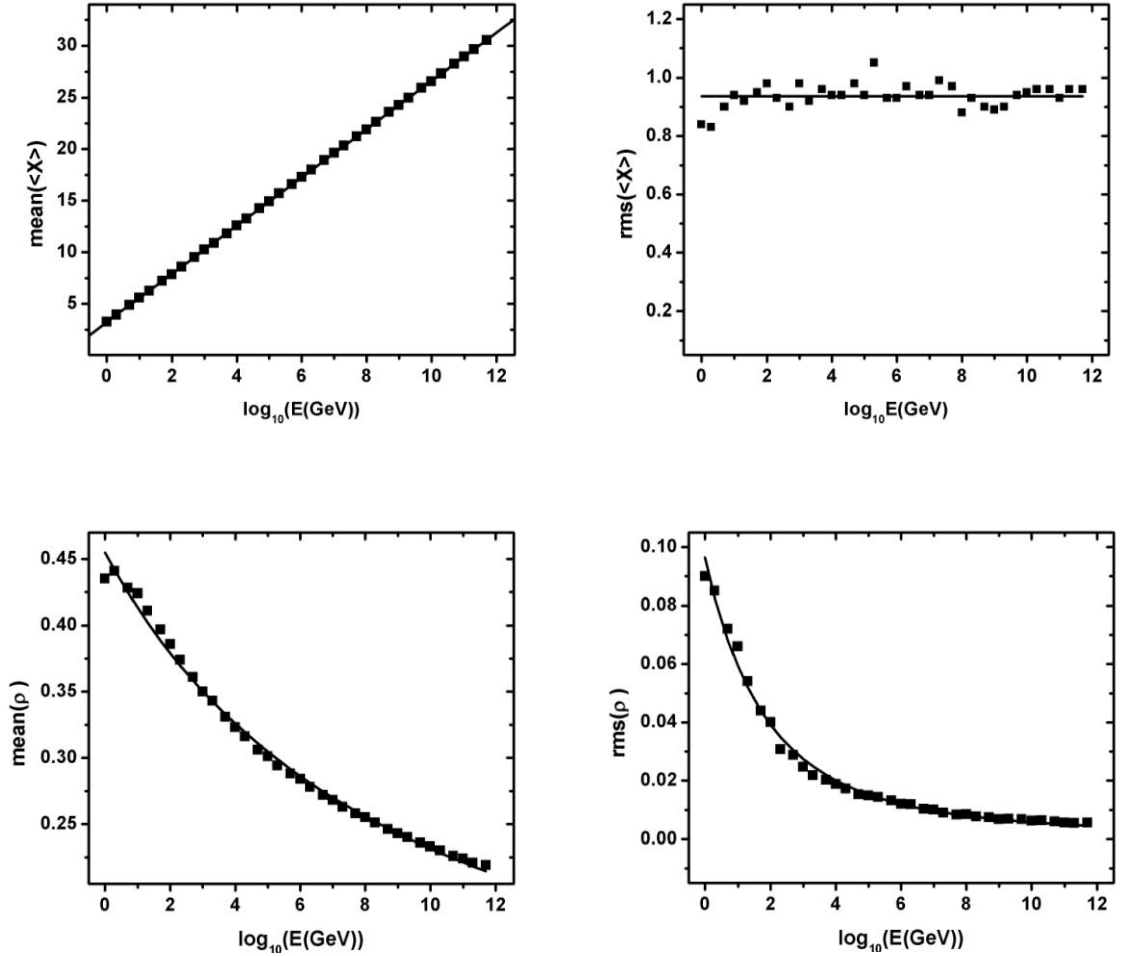
Figure 2.4: Dependence on energy of the parameters defining the longitudinal shower profile. Upper panels: Mean value of $<X>$ (left) and rms value of $<X>$ (right); units are radiation lengths. Lower panels: Mean value of ρ (left) and rms value of ρ (right). The lines are the result of the fits described in the text.

Electromagnetic sub-showers of UHECR showers are essentially induced by the decay photons of π^0 secondaries. As these are scalar mesons, the decay photons are emitted isotropically in the π^0 rest frame: the distribution of the cosine u of the angle of the centre-of-mass photon momentum with the laboratory π^0 momentum is uniform. Applying the proper Lorentz transformation and neglecting the π^0 mass in comparison with its energy, a π^0 of energy E produces two photons of energies $E^{\pm}=\frac{1}{2}E(1\pm u)$. In the case of π^0 decays, X_0, being the smaller of two numbers having an exponential distribution of scale $9X_0/7$ is observed to have an exponential distribution of scale $9X_0/14$ as expected (Figure 2.5).

Fits of the energy dependence of the mean and rms values of $<X>-X_0$ and ρ have again been performed over the whole range (2.5 to 10^{11}

GeV). They are illustrated in Figure 2.6 and their parameters are listed in Table 2.2.
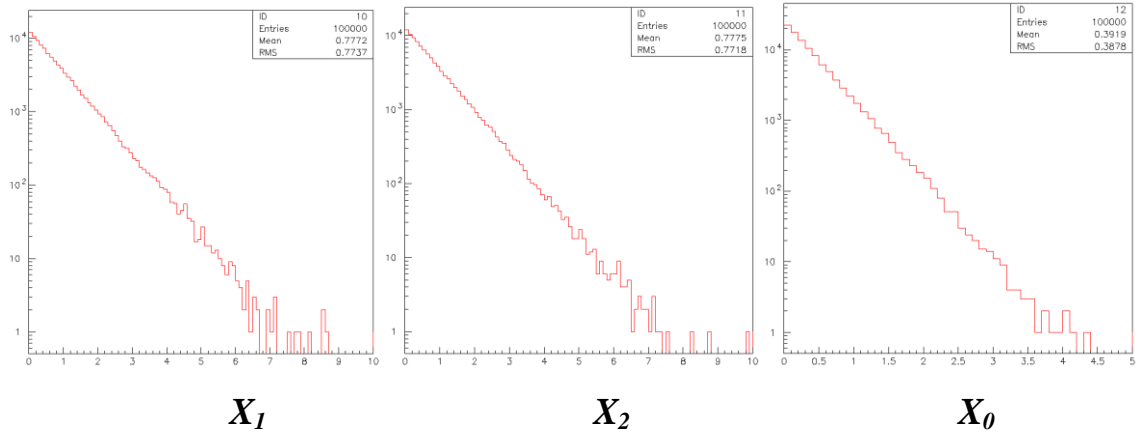
Figure 2.5: Distribution of X_0 in the case of π^0 decays. The left panels (X_1 and X_2) are for the decay photons. The right panel (expanded scale) is for the smaller of X_1 and X_2.
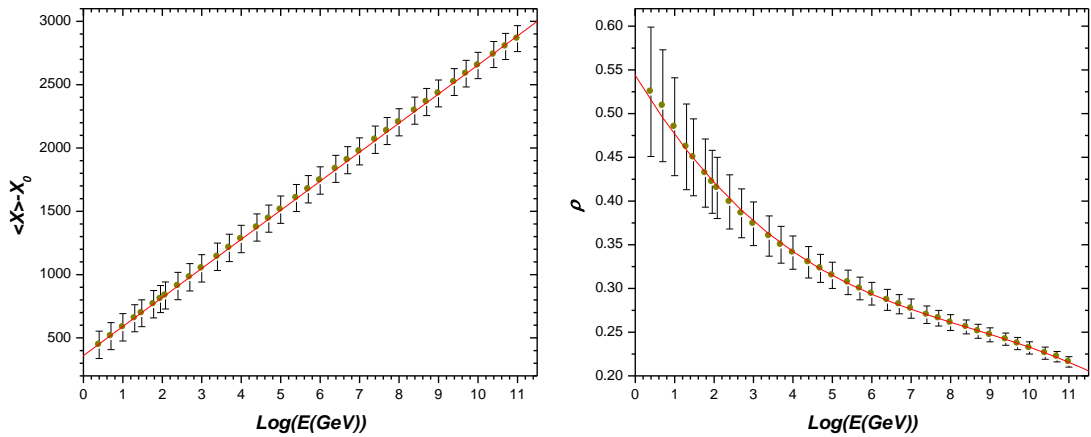
Figure 2.6: Dependence on the decimal logarithm of the energy of the mean values of $<X>-X_0$ (left panel) and ρ (right panel) for neutral pions. The vertical bars are not error bars but correspond to $\pm$ the rms values of the distributions. Thicknesses are measured in percent of a radiation length.

Table 2.2: Parameterization of the simulated shower profiles at energies between 2.5 GeV and 10^{11} GeV using forms $A+Bx+Cx^2+Dx^3$ with $x=log_{10}(E/10^{10}MeV)$.

		A	B	C	D
Electrons	Mean $<X>-X_0$	3.91	2.30	-	-
	Mean $\rho(\%)$	51.5	–6.7	0.6	$-2.4\ 10^{-2}$
	Rms $<X>-X_0$	0.94	-	-	-
	Rms $\rho(\%)$	6.77	-2.20	0.28	–0.01
Photons	Mean $<X>-X_0$	3.45	2.30	-	-
	Mean $\rho(\%)$	55.2	–7.7	0.7	$-2.9\ 10^{-2}$
	Rms $<X>-X_0$	0.81	-	-	-
	Rms $\rho(\%)$	6.90	-2.37	0.31	–0.01
π^0	Mean $<X>-X_0$	3.60	2.30	-	-
	Mean $\rho(\%)$	54.4	–7.4	0.7	$-2.78\ 10^{-2}$
	Rms $<X>-X_0$	1.07	-	-	-
	Rms $\rho(\%)$	7.92	-2.68	0.35	$-1.5\ 10^{-2}$

2.2 Transverse shower development

The transverse profile of an electromagnetic shower induced by a π^0 decay is the result of two effects: the transverse momentum acquired by each photon in the decay process and the transverse development of each of the two showers induced by the photons. The former can be calculated exactly while the latter is described phenomenologically in terms of the so-called Molière radius.

2.2.1 π^0 decays

In the π^0 rest frame, the photon momenta are $\frac{1}{2}m$, m being the π^0 mass, with longitudinal and transverse components equal to $\pm\frac{1}{2}mu$ and $\pm\frac{1}{2}m\sqrt{(1-u^2)}$ respectively (we recall that u is the cosine of the angle of the centre-of-mass photon momentum with the laboratory π^0 momentum, $\boldsymbol{p}$). In the laboratory frame, the longitudinal momenta become

$½m(\pm\gamma u+\gamma\beta)=½E(\beta\pm u)$ with $\gamma=E/m$ and $\beta=p/E=\sqrt{(1-m^2/E^2)}\sim1$. Hence the angles $\alpha^\pm$ made by the photon momenta with respect to the pion momentum in the laboratory obey $tan\alpha^\pm=\pm\sqrt{(1-u^2)}/(1\pm u)/\gamma$.

Therefore $tan\alpha^+=\sqrt{\{(1-u)/(1+u)\}}/\gamma$ and $tan\alpha^-=\sqrt{\{(1+u)/(1-u)\}}/\gamma$.

However, geometry is not the only relevant factor in the making of the lateral distribution function (LDF): the quantity of energy deposited is also essential. To a good approximation, we may assume that the electron/photon energy that reaches ground is fully absorbed in the detector (it is a sensible approximation for the Auger Cherenkov detectors, not for a scintillator array). Then, the lateral distribution function is obtained by weighing each impact with whatever energy is left in the longitudinal development of the photon shower when it reaches ground.

As the transverse momentum distribution of decay photons in the pion rest frame is invariant, the lateral scale of the LDF resulting from the decay of neutral pions into photons is proportional to the altitude $\Delta z=(z-z_{ground})$ above ground and inversely proportional to the primordial pion momentum (or energy when the pion is relativistic). Figure 2.7 shows the ground number and energy densities, $dN/(2\pi rdr)$ and $dE/(2\pi rdr)$ as a function of r, the distance (measured in metres) between the photon impact on ground and that of the pion momentum, in the case of a vertical pion of 1 GeV decaying at an altitude of 1 km above ground. As explained above, in the case of energy density, each value of r is given a weight equal to the remaining energy of the photon shower. Ignoring such weights, the distribution takes the simple form $1/(R_1^2+r^2)^2$ with $R_1=140$ m. Indeed,

$r^{+2}=\Delta z^2 tan^2\alpha^+=(\Delta zm/E)^2(1-u)/(1+u),$

$u=\{(\Delta zm/E)^2-r^{+2}\}/\{(\Delta zm/E)^2+r^{+2}\}$

and $dN/dr^{+2}=du/dr^{+2}\approx1/(R_1^2+r^2)^2$ with $R_1=m\Delta z/E=0.14$ km$=140$ m.

We see from Figure 2.7 that the number density obviously obeys the above relation while the energy density is significantly steeper. This is because oblique photon showers are more developed than vertical photon showers: the amount of energy deposited in the ground detectors is therefore larger for vertical showers, namely for smaller values of r, and smaller for larger values of r.
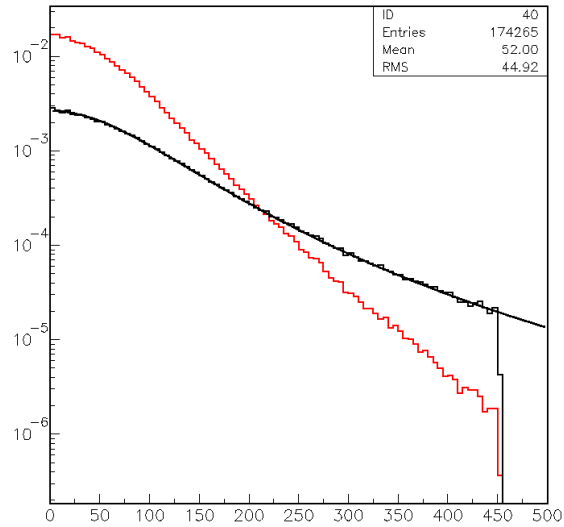
Figure 2.7: The ground number (black) and energy (red) densities are shown as a function of *r*, the distance between the photon impact on ground and that of the pion momentum, in the case of a vertical pion of 1 GeV decaying at an altitude of 1 km above ground. The line shows a fit to the relation given in the text.

2.2.2 Photon showers

In addition to the smearing due to decay, each photon generates an electromagnetic shower having a lateral extension characterized by the Molière radius. To a good approximation, the Molière radius is an energy-independent constant equal to the radiation length multiplied by 21 MeV and divided by the critical energy [12]. Therefore it scales with the reciprocal of the atmospheric pressure. As the atmospheric pressure depends on altitude, it varies during shower development. However, in practice, we can retain the value at ground to be a good approximation because showers that are born at very high altitude will not reach ground: those that do, reach maximum development near ground. A form $1/(R_2{}^2+r^2)^2$ gives a good description of the global lateral extension of the energy density on ground. The radius R_2 has to be adjusted in such a way that the energy deposited outside a cylinder of radius equal to the Molière radius be ~10% of the primordial photon energy [12]. The result is that R_2 must be equal to $R_{Molière}/3 = 19.7\ m$ (Figure 2.8). Combining both effects, Figure 2.9 displays the *r* distribution of the energy density for a 1 GeV neutral pion decaying 1 km above ground. The distribution is found to be reasonably well described by a form $1/(R*^2+r^2)^k$ with an index *k* and a radius *R** that depend on *E/Δz* as illustrated in Figure 2.10. The corresponding parameters are given below:

$R* = -2.0 + 38.4/(0.21+X)$ if $X<1.5$ and $R*=20$ if $X \geq 1.5$;

$k = 1.25 + 2.04/(0.79+X)$ if $X<1.9$ and $k=2$ if $X \geq 1.9$.

with $X = log_{10}(E/\Delta z)$

As we later use only the shape of such lateral distribution functions, we normalize them in such a way that the total energy integrated on ground is equal to unity. Namely, we use a form $A/(R*^2+r^2)^k$ with $A=(k-1)R*^{2(k-1)}/\pi$.
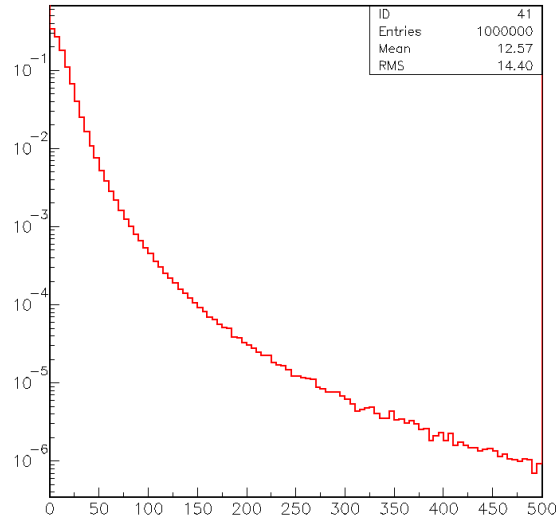
Figure 2.8: r-dependence of the ground density for a vertical 1 GeV vertical photon converting 1 km above ground (see text).
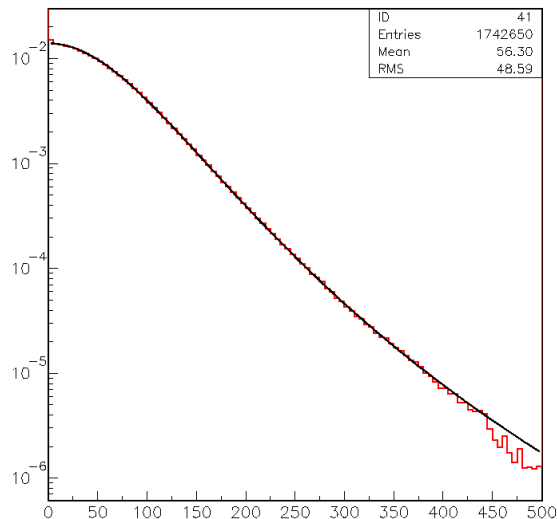
Figure 2.9: Lateral distribution function (dN/dr^2) for a 1 GeV/c neutral pion decaying 1 km above ground.
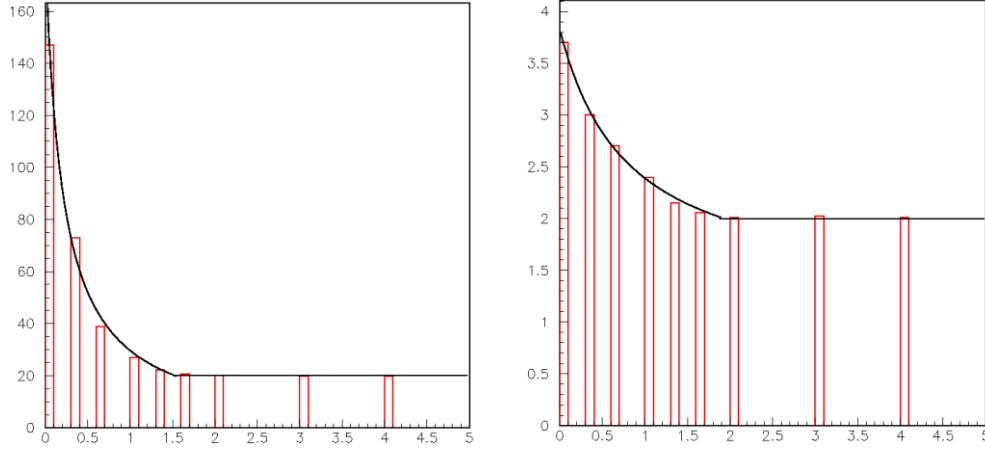
Figure 2.10: Dependences of index *k* (left) and radius *R** (right) on $log_{10}(E/\Delta z)$ with *E* in GeV and *Δz* in kilometres.

The average transverse momentum given to a photon is *½m<(1– u²)^{½}>= 140/4=35 MeV* while the transverse momentum given to the parent *π⁰* at the time of production is *~400 MeV*. Moreover, the Molière radius is small enough not to cause an excessive broadening of the *π⁰* lateral distribution function. We are therefore dealing with a small correction (especially since transverse momenta add up in quadrature), which justifies the approximations that have been used.

2.2.3 Procedure to generate *π⁰* showers

The depth of the conversion of the first photon to convert is chosen with an exponential distribution of scale *9X₀/14* as discussed earlier (Figure 2.5) and the longitudinal *π⁰* shower profile is chosen according to the parameterisation given in Section 2.1 starting from that point. One then evaluates the energy *ΔE* that remains when the *π⁰* shower reaches ground. In Sections 2.2.1 and 2.2.2 it has been assumed, for this reason, that the first photon converts at altitude *z* and the second photon at an altitude *z–δz* where *δz* was chosen at random with an exponential depth distribution of scale *9X₀/7*.

In a first attempt, we have tried to handle *π⁰'s* globally, using a single Gaisser Hillass profile. Following the results presented in Sections 2.2.1 and 2.2.2, we proceeded as follows to generate the lateral distribution function: the radius *R** and the index *k* are calculated as a function of *E/Δz* according to the parameterisations given in Section 2.2.2. Then, 10 values

of r are chosen at random with the distribution[1] $dN/dr^2=1/(R^{*2}+r^2)^k$ with a weight $\Delta E/10$. Note that the r dependence of what remains of the energy density on ground resulting from the larger shower development in the case of oblique incidence has already been taken into account in the parameterisation. Here, $\Delta E/10$ is therefore a common normalization factor that applies to each r value. We have checked that this procedure is consistent with dealing with each photon separately, without using the parameterisation. An example is shown in Figure 2.11. In the worst case, $E/\Delta z=1$ (in units of GeV/km), namely with little energy reaching ground, the deviation between the two methods reaches ~20%. We have identified the cause of such a deviation as being the result of the parameterisation. The sum of two Gaisser Hillas profile is not, in general, a Gaisser Hillas profile. In our earlier studies of the LPM and other effects, the differences were largely irrelevant. Here, on the contrary, the tail energy ΔE, which may represent a minute fraction of the initial energy, defines the scale of the energy density on ground. We implemented a change in the algorithm, which corrects for the differences as a function of energy. This was successful in making the two tails equal. However, differences between the two longitudinal profiles subsisted in the first interaction length. As this is inherent to the parameterisation adopted, it would take another cosmetic change to correct for it. Finally, we preferred giving up the global treatment of π^0 decays and decided to deal separately with each of the two photon showers. It must be realized that the difficulties that we have encountered are not specific to our method. The dominance of the shower tails in the lateral distribution function is a very general feature that is present, but largely hidden, in all simulation codes.

In the case of a pion having a momentum making an angle θ with the vertical, the lateral distribution function is first evaluated in the plane perpendicular to the pion momentum and containing its impact on ground. Note that $E/\Delta z$ must now be replaced by $E\cos\theta/\Delta z$. Indeed, the contribution of the decay geometry to the LDF gives the $\cos\theta$ factor and that of the Molière radius depends only on the atmospheric pressure on ground, which does not depend on θ. It is only the energy weighing procedure that depends on the depth (in g/cm^2), rather than on Δz, but the parameterisation does not. The energy density on ground is then obtained by projection,

---

[1] A nice feature of this distribution is that it is simply generated by a form $r=R^*\sqrt{(1/rand^{1/(k-1)}-1)}$ where *rand* is a number chosen at random in the interval [0,1].

resulting in an ellipse having its major axis expanded radially by a factor *1/cosθ*.
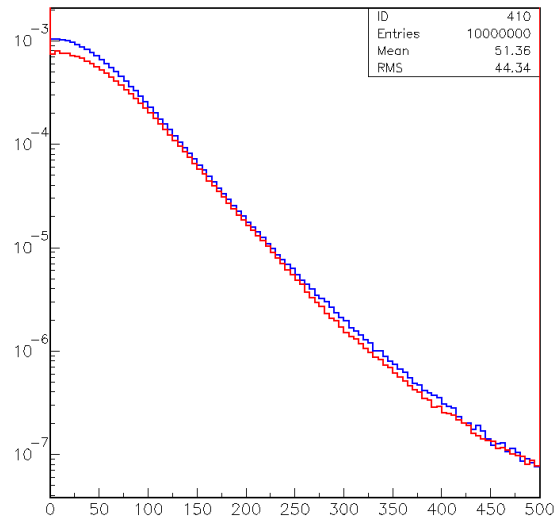
Figure 2.11: Lateral distribution functions obtained for a 10 GeV π^0 decaying at an altitude of 10 km (*E/Δz=1*) for a global π^0 treatment (blue) and a separate treatment of the decay photon (red). The difference, ~20%, is mostly due to different tail energies.

3. HADRONIC INTERACTIONS

3.1 Generalities

3.1.1 Longitudinal phase space

There is no doubt that the main feature of hadronic interactions is the peculiar distribution of the produced secondaries in phase space: a uniform distribution in rapidity and a steeply falling distribution in transverse momentum. L. Van Hove was first to state it explicitly [14] and to introduce the concept of what he called "longitudinal phase space".

Let us recall here that rapidity is to a Lorentz transformation what the polar angle and angle of rotation are to a space rotation around an axis. Namely a Lorentz transformation along *z* with velocity *β=tanhα* is a rotation of angle *iα* mixing space *(z)* and time *(it*, *t* being the time):

z'=zcoshα+tsinhα=zcos(iα)–itsin(iα)

t'=zsinhα+tcoshα, implying it'=zsin(iα)+itcos(iα).

In particular, a uniform rapidity distribution remains uniform after a Lorentz transformation, the same way as an isotropic distribution remains isotropic after a rotation. Similarly, a Lorentz transformation is a translation in rapidity, the same way as a rotation is a translation in polar angle. When applied to the energy-momentum four-vector *(E, p_z)*, a Lorentz transformation increases, $tan^{-1}(iE/p_z)=itanh^{-1}(E/p_z)=½iln\{(E/p_z–1)/(E/p_z+1)\}$ by *iα*, the same way as a rotation increases the polar angle $tan^{-1}(y/x)$ by *α*. As a function of *E* and *p_z*, the rapidity reads therefore $½ln\{(E–p_z)/(E+p_z)\}=ln\{m_T/(E+p_z)\}$ where m_T is the transverse mass, $m_T=(m^2+p_T^2)^{½}$ with *m* being the mass and *p_T* being the transverse momentum. For massless particles, *$p_z/E=cosθ$* and the rapidity becomes the pseudo-rapidity, *$η=½ln\{(1–cosθ)/(1+cosθ) =lntan(θ/2)$*.

It was only after 1971, when the ISR started operation at CERN, that sufficient energy was available (up to 62 GeV in the centre of mass system) to give clear evidence for longitudinal phase space. Transverse momentum limitation was understood (rightly so) as a geometric effect, the limiting transverse momentum being of the order of 200 MeV/c, namely the Planck constant *ℏ* divided by the proton radius, *~1 fm*. However, at that time one thought (wrongly so) that this limitation was so strict that it would absolutely prevent the production of large transverse momenta. Indeed, large transverse momentum production is rare enough for us to ignore it in the present work. Yet it is the process that allowed probing matter at short

distances and paved the way to QCD and what was then called the "new physics", namely the Standard Model.

In the limit of infinite momentum, the invariance of a uniform rapidity distribution under Lorentz transformations implies that there exists no privileged momentum frame. Feynman was first to suggest a relation between such behaviour and a field theory of elementary hadron constituents that he called partons [15].

3.1.2 Universality, leading effect, effective energy

When the ISR started operation, the structure of proton-proton final states could be studied in some detail. Evidence for longitudinal phase space was now clear and four additional general features were clearly revealed [16]:

– the slow increase with energy of the total cross-section;

– the existence of diffractive events, where one of the protons is excited, its debris being separated in rapidity from central production;

– the existence of short range rapidity correlations, well described in terms of clusters, of which only part are resonances;

– the presence of a leading effect implying that the largest rapidity particle essentially carries the quantum numbers of the initial proton.

These features have been the subject of numerous studies in the subsequent years and paved the way to the proton-antiproton collider experiments, of which UA5 [17] is a reference in the field. In particular, universality was noted between hadronization processes taking place in different interactions, such as electron-positron and proton-proton collisions. It was made particularly clear when the leading effect was subtracted [18] by using the concept of effective energy.

A phenomenological synthesis of experimental knowledge has been made in Monte Carlo descriptions of hadronic interactions used as simulations of various collider or cosmic ray experiments. In the present work, we refer in particular to the so-called HDPM code [19].

3.1.3 Partons and QCD

In the late seventies, Quantum Chromodynamics (QCD) became unanimously accepted as the theory of the strong interaction [20]. It assumes nothing more than an exact exchange symmetry between quarks of a same flavour, SU(3) colour, and gauge invariance. According to QCD, the elementary fermion fields are quarks of different flavours (three isospin doublets of electric charges 2/3 and −1/3: *u-d*, *c-s*, *t-b*) and the gauge bosons form a vector octet, the gluons. Contrary to SU(1), where the only possible coupling is the radiation of a gauge boson by a fermion, SU(3) includes also triple and quadruple couplings between gluons. At short distances, where reliable and accurate perturbative calculations are possible, the validity of QCD has been checked to better than a percent in many different sectors. However, at large distances, we are still unable to perform sensible calculations. Unfortunately, the interactions which are of relevance to the development of cosmic ray showers are low transverse momentum, large distance interactions: we can only hope for ad hoc models to describe them.
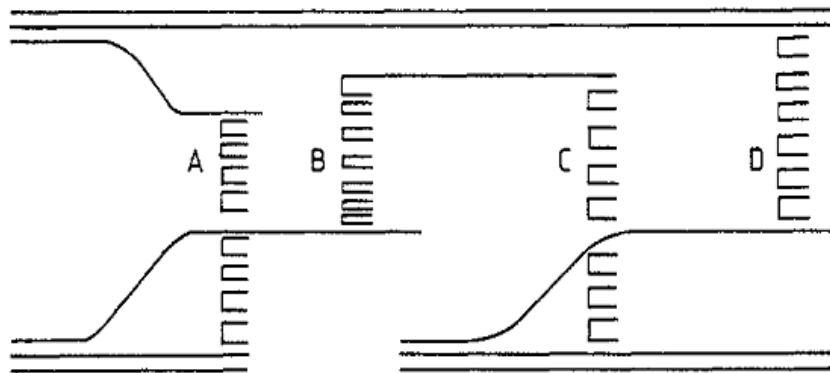
Figure 3.1 Dual multichain parton model representation of a two nucleons collision.

Yet, the ideas underlying QCD have been used to inspire such models. They allow for a qualitative understanding of the main features that have just been reviewed, in particular longitudinal phase space, universality of hadronization processes and leading effect. Such a commonly used model is the so-called dual parton model [21]. A general feature, common to all QCD-inspired models, is the description of particle production as a set of radiations occurring at closely spaced rapidities along a path (chain) connecting the constituents of the initial state hadrons, which are very distant in rapidity. Such a concept was already present before

QCD in the frame of what was called the multiperipheral model [22]. In the dual parton model, the same idea is rejuvenated in the parton language, however ignoring gluons, at least in an explicit form. Figure 3.1 shows a typical diagram.

3.2 Overview of the method

3.2.1 General strategy

The main idea of the present approach, the replacement of sub-showers by a parameterized description, implies the definition of two different energy ranges.

A low energy range, 1 to 10^3 GeV, is used to simulate proton induced showers without making use of any parameterisation of the hadronic sub-showers but making full use of the parameterisation of neutral pion showers introduced in the preceding chapter. In this energy range, the number of shower particles is small enough to follow each charged pion separately while keeping the computing time reasonable. Simulations are made by generating 10000 showers at each node of a grid in energy, altitude above ground and zenith angle. At each of these nodes, the longitudinal profile and the lateral distribution functions of electron/photons and of muons are parameterised. The parameters are evaluated for each shower and their mean values are calculated. Once this is completed, shower parameterisations can be performed by interpolation of the parameters between the nodes.

In a second phase, one calculates the parameters in the high energy range, above 10^3 GeV. One proceeds by iterations, in steps of half a unit of $\log_{10}E$, to extend the grid to higher energies. In this second step, one only follows secondaries having energies in excess of a predefined threshold of *f* % of the primary energy, and replaces each lower energy interacting pion by a parameterized sub-shower.

At this stage, one is in a position to generate large quantities of ultra high energy showers while playing with the parameters that govern the physics of the first interactions, in particular the nuclear model used to distinguish iron nuclei from protons.

Many simplifications are being made in the description of the hadronic interactions, the most important being the assumption that all produced secondaries are pions. This is far from being the case; there is in

particular an important number of kaons among the secondaries. Moreover, many of these are decay products of resonances. The hope, in the present simplified description, is that the all-pion approximation can be used to describe reality, possibly at the price of adjusting parameters such as the pion decay time in a ad hoc manner.

3.2.2 Longitudinal development: Atmospheric model, energy losses and multiple Coulomb scattering

The longitudinal development of the showers requires a description of the atmospheric pressure and of the electromagnetic interactions of charged particles with the atmosphere, causing energy losses and multiple Coulomb scattering.

An exponential dependence of the atmospheric pressure as a function of altitude of the form $p=p_0 exp(-z/\Delta z)$ has been retained. As illustrated in Figure 3.2, using $\Delta z=6.83$ km and $p_0=1100$ g/cm^2 gives a good description of the standard atmospheric profiles mentioned in Reference 23.

Two kinds of energy losses are taken into account: ionization losses and radiation losses. They are supposed to be the same when the incident energy E is equal to the critical energy E_{crit} taken as input parameter.

The differential ionization loss is taken to be *1.8 MeV $g^{-1}cm^2$* for $\beta\gamma =2$. For $\beta\gamma >2$ it increases by *0.11 MeV $g^{-1}cm^2$* for each unit of *lnE*. For $\beta\gamma<2$ the differential ionization loss is taken to be inversely proportional to E, therefore inversely proportional to $\gamma=\sqrt(1+\beta^2\gamma^2)$ and equal to $\sqrt5$ *1.8 MeV $g^{-1}cm^2 /\gamma$*.

The differential radiation loss is equal to E/X^*_{rad} where X^*_{rad} is an effective radiation length. The factor $1/X^*_{rad}$ is calculated from the definition of the critical energy: $1/X^*_{rad}=1.8$ *MeV $g^{-1}cm^2/E_{crit}$*. The values retained for the critical energies are *74'000 GeV* for protons, *1'657 GeV* for pions and *950 GeV* for muons.

Multiple scattering in a slice of *x g/cm^2* is calculated using a mean transverse momentum kick of $13.6\sqrt(2x/X_{rad})$ *MeV* where X_{rad} is the radiation length in air, *36.66 g/cm^2*. Projection on two orthogonal planes containing the particle momentum gets rid of the factor $\sqrt2$: the transverse momentum kick in each plane is therefore taken to have a Gaussian distribution around 0 of variance $13.6\sqrt(x/X_{rad})$ *MeV*.
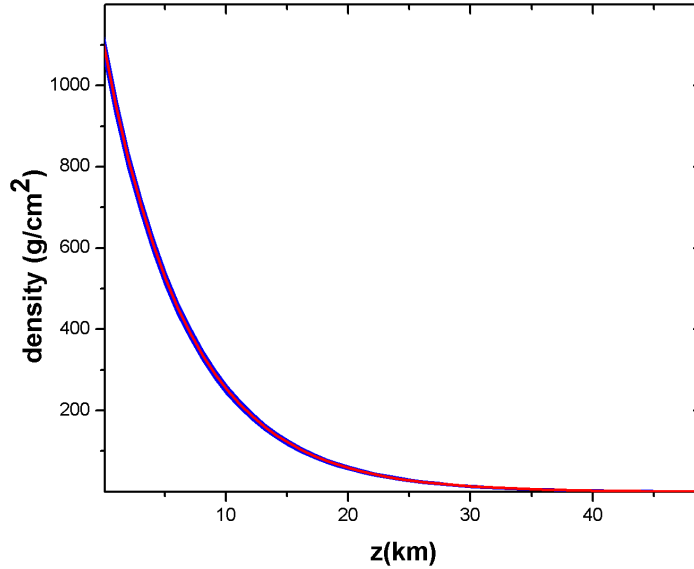
Figure 3.2: Dependence on altitude of the atmospheric density. The red curve is the exponential used in the present work: the blue curves are from Reference 10 for different seasons.

3.3 Nucleon-nucleon interactions

3.3.1 Generalities

The general picture is that which emerges from collider measurements such as that of the UA5 experiment [17]: two leading particles, each taking some 25% of the available cms energy, separated from a central rapidity plateau by two rapidity gaps. The rapidity plateau is characterized by a rather uniform density distribution and important short range rapidity correlations that are well described by clusters. These are seen in charge as well as in rapidity and transverse momentum. Transverse momentum distributions are steeply falling, first exponentially as expected from the Fourier transform of a disk, and later as a power law as expected from interacting point like constituents.

In the simulation of nucleon-nucleon interactions, the approach used in existing codes, such as HDPM, is to start from what is known, i.e. central production, and hope to get the forward production, which is essentially unknown, right. While being a very sensible approach, it does not allow for acting directly in a simple way on parameters such as the inelasticity. Here, instead, the inelasticity is taken as an adjustable parameter and the shape of the rapidity plateau is accessible in a transparent way.

The general algorithm used in the code is as follows:

a) Choose the fractions η_1 and η_2 of the cms energy $\sqrt{s}$ carried by the leading particles (which retain the identities of the projectile and target particle respectively). The cms energy available for central production is therefore $\sqrt{s}^*=(1-\eta_1-\eta_2)\sqrt{s}$. The leading particles do not carry any transverse momentum, and so do therefore globally the central secondaries, the longitudinal cms momentum and energy of which are now defined.

b) Depending on $\sqrt{s}^*$, choose the number of central clusters and the numbers of pions in each cluster in such a way as to reproduce the desired multiplicity distribution. Once this is done choose the width of the rapidity plateau in such a way as to conserve energy. Clusters are then distributed evenly at equal intervals on the plateau. A final adjustment of the cluster momenta is made to fine tune energy momentum conservation.

A library of clusters containing between two and seven pions is created. The transverse momentum distribution of the pions is chosen to reproduce that desired for central pions, the clusters being given no transverse momentum of their own. While the width of the rapidity plateau and the cluster rapidity density increase linearly with $\log s^*$, implying that the cluster multiplicity increases quadratically with $\log s^*$, the number of pions per cluster and the transverse momentum distribution are nearly constant, increasing only slightly with $\log s^*$.

3.3.2 Central clusters

For a given number k of pions, central clusters are built by choosing the pion transverse momenta at random with a distribution of the form $dN/dp_t \approx (p_t/p_0)(1/[1+p_t/p0])^n$. The mean transverse momentum is $<p_t>=2p_0/(n-3)$. Typically, $p_0=1.3$ GeV and $n\sim 10$. Therefore, we fix $n=10$ and use p_0 to scale the transverse momentum distribution as desired. The default value uses

$p_0\,(GeV)=3.5<p_t>$ with

$$<p_t>= 0.3+0.00627\,ln(4s^*) \qquad\qquad \text{for } 2\sqrt{s}^* <132$$

$$\{0.442+0.0163\,ln(4s^*)\}^2 \qquad\qquad \text{for } 2\sqrt{s}^* >132$$

Figure 3.3 displays the transverse momentum distribution for $<p_t>=0.44$ GeV. The blue curve is of the form $dN/dp_t \approx (p_t/p_0)(1/[1+p_t/p_0])^{10}$ where

$p_0=3.5<p_t>=1.47$ GeV. The red histogram is the result of the algorithm used in the code.

The case of clusters containing only two pions is particularly simple: the momenta are chosen back to back with an isotropic distribution. The case of clusters containing at least three pions is dealt with as described below.
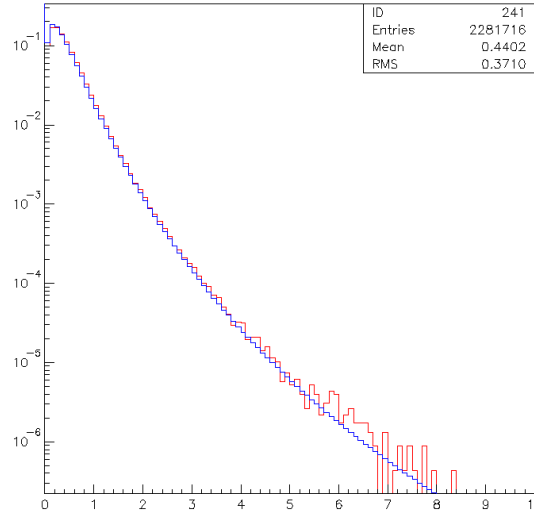
Figure 3.3: Transverse momentum distribution. The result of the code (red) is compared to the analytical form (blue) given in the text.

The azimuthal angles of the pion momenta are chosen at random between $-\pi$ and $+\pi$ and are adjusted in order to cancel the total transverse vector momentum. The adjustment is made by changing each azimuth φ_i by a quantity

$\Delta\varphi_i = (Acos\varphi_i + Bsin\varphi_i)/p_{ti}$. The operation is repeated 3 times. In some cases, it is not possible to cancel the total transverse momentum by simply changing the azimuthal angles. In such cases (defined as having a total transverse momentum in excess of 1 MeV) a new choice of transverse momentum is made.

Pion longitudinal momenta, p_l, are calculated in the rest frame of the cluster. Choosing θ, the angle made by a pion momentum with the lab incident momentum, at random with a uniform $cos\theta$ distribution one calculates $p_l=p_t/tan\theta$ and boosts the whole cluster longitudinally in order to bring it to rest. The boost leaves the transverse momenta unchanged and does not too much disturb the isotropy of the cluster fragmentation as can be seen from Figure 3.4 left, which displays the final $cos\theta$ distribution, seen to be nearly uniform.
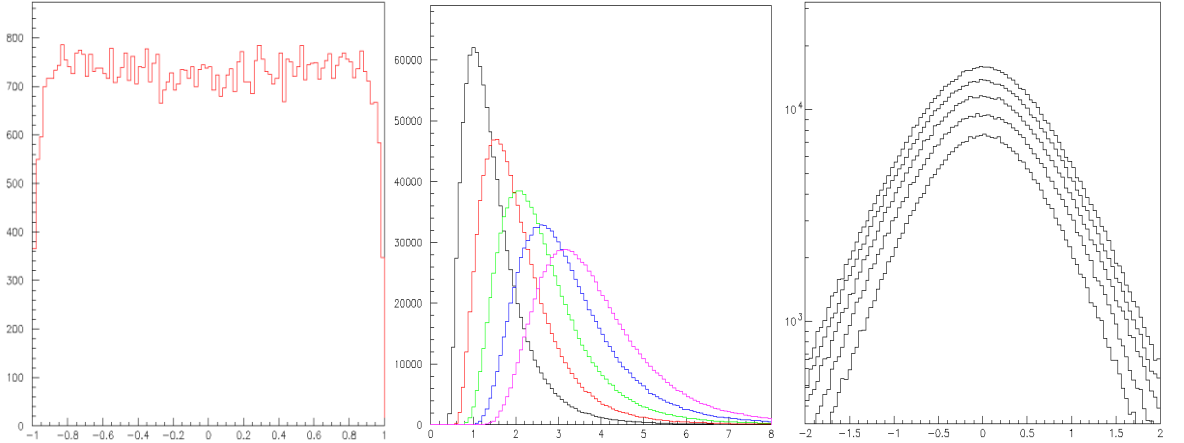
Figure 3.4 Left: *Cosθ* distribution in the cluster rest frame for clusters containing at least three pions. Centre: Cluster mass distributions for clusters containing *3* to *7* pions separately. Right: Distribution of pion rapidities in the cluster rest frame for clusters containing *3* to *7* pions separately.

Figure 3.4 centre displays cluster mass distributions for clusters containing *n=3* to *7* pions separately. The value of *$<p_t>$* was taken to be 0.4 GeV. To a very good approximation the mean values *$<M>$* depend linearly on multiplicity *n*: *$<M>=0.58n-0.25$*. Figure 3.4 right displays the distributions of pion rapidities for each multiplicity separately in the cluster centre of mass system. They are nearly Gaussians with an rms deviation of ~$1/\sqrt{2}$ units of rapidity, independently from multiplicity.

3.3.3 Nucleon-nucleon and pion-nucleon interactions

The calculations are made in the centre of mass system of the interacting nucleons having incident energies E_{inc1} and E_{inc2}. The energies carried away by the leading particles are written $\eta_1 E_{inc1}$ and $\eta_2 E_{inc2}$ where η_1 and η_2 are chosen at random with Gaussian distributions having a mean value of 0.6 and an rms value of 0.15. The Gaussians are truncated in order for the leading particle energies to exceed the particle rest mass but not to exceed the initial particle energy. The total energy available for central production is $\sqrt{s}*= \sqrt{s}-\eta_1 E_{inc1}-\eta_2 E_{inc2}$. An effective energy $\sqrt{s_{eff}}$ is defined as $\sqrt{s_{eff}} = \sqrt{s}*/(1-<\eta_1>/2-<\eta_2>/2)$. As mentioned earlier, it makes more sense to use $\sqrt{s}*$ rather than $\sqrt{s}$ to decide on the properties of central production; it is therefore necessary to define $\sqrt{s_{eff}}$ in order to use the formulae given in References 19 and 23 as a function of $\sqrt{s}$. The pion transverse momentum distribution is taken from Reference 23 as are the

mean values of the total and charged multiplicity distributions. The number of pions per cluster is chosen at random between 2 and 7 with a Gaussian distribution having a mean value of *1.6+0.21 lns** and an rms value of 1. The total number of clusters n_{cl} is chosen at random with an *ad hoc* distribution meant to properly reproduce the final multiplicity distribution. Its mean value, $<n_{cl}>$, is taken to be the ratio of the mean values of the total multiplicities and of the number of pions per cluster. For convenience, a Gaussian distribution in *ln(n$_{cl}$/<n$_{cl}$>+1)* is used rather than a binomial distribution. Its mean value is *{16+0.75l–0.31l^2}/25* and its rms value is *{5.7–0.56l+0.27l^2}/25* where $l=log_{10}(\sqrt{s_{eff}})$. Pions are defined to be charged or neutral at random in the ratio given in Reference 23. Figure 3.5 compares the charged multiplicity distributions obtained here with those of Reference 23.
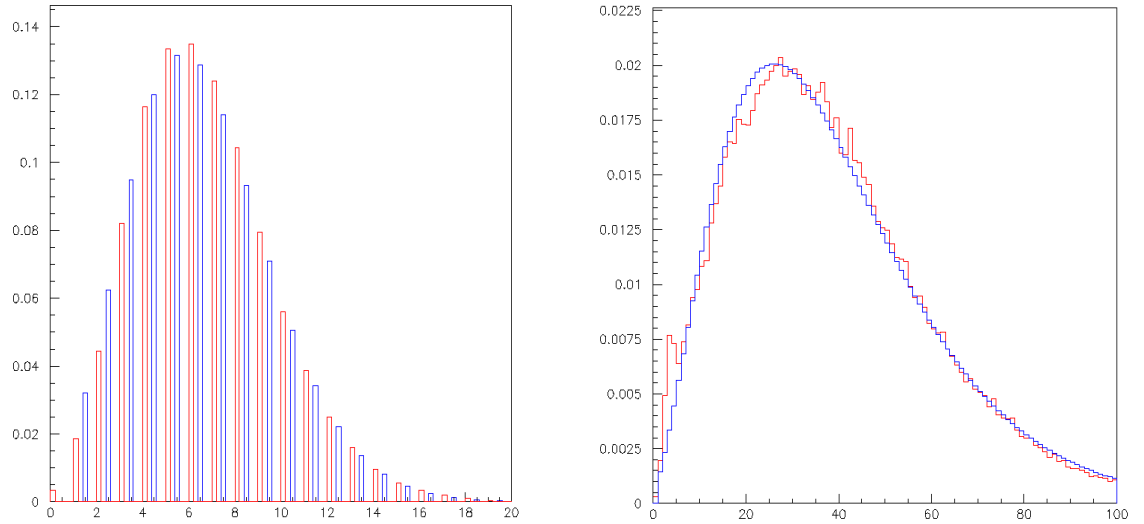
Figure 3.5: Comparison of the charged multiplicity distributions obtained here (red) with those of Reference 23 (blue). Incident proton energies are 10^2 (left) and 10^6 (right) GeV.

The cluster rapidity distributions are chosen according to a linear combination between a rectangular plateau (weight 0.75) and a triangular plateau (weight 0.25). They are then boosted to where they belong to (in general, η_1 and η_2 are different and the central production rest frame is not at rest in the global centre of mass frame used here). A final tuning of the pion rapidities achieves exact energy momentum conservation. Figure 3.6 compares the rapidity distributions obtained here with those of Reference 23.

Finally, pion-nucleon interactions are treated the same way as nucleon- nucleon interactions apart from the values taken by the interaction cross section which are taken from Reference 23.
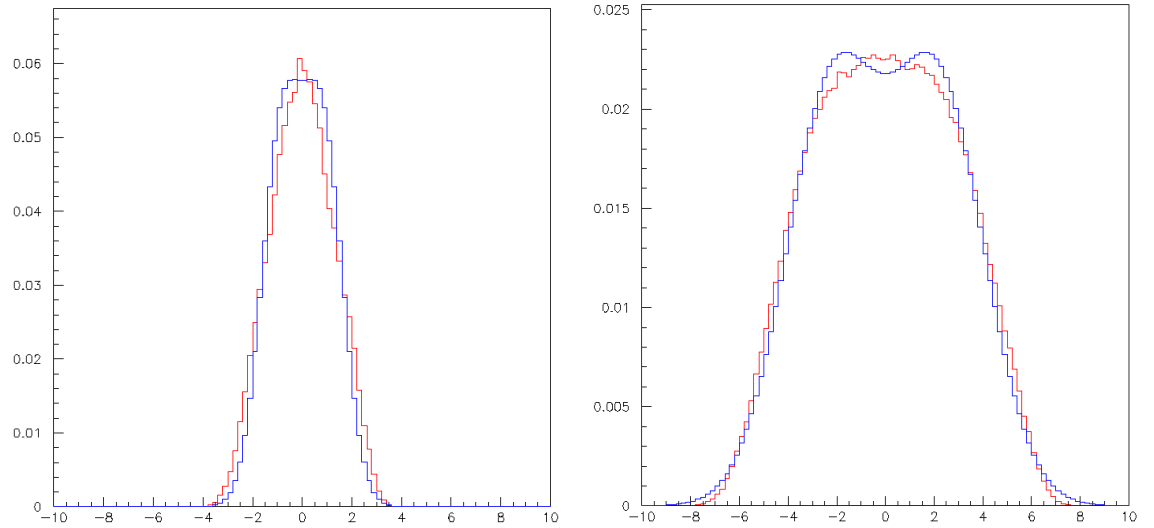
Figure 3.6: Comparison of the pion rapidity distributions obtained here (red) with those of Reference 23 (blue). Incident proton energy are 102 (left) and 106 (right) GeV.

3.4 Nuclei

3.4.1 Generalities

There exists no exact treatment of nuclei interactions. A standard approach, which is used here, is that of the Glauber model [24]. A first useful concept is that of wound nucleons: when two nuclei collide only some of their nucleons interact. These are defined as having their projection on a plane normal to the incident momentum contained within the intersection of the projections of both nuclei on the same plane. The calculation is straightforward once the nucleon radius and the Woods-Saxon distribution of nucleons inside the nuclei are known. The interaction of wounded nucleons is treated as a cascade of each of the projectile nucleon on the set of wound nucleons that are on its path. This approximation is obviously very crude. It does not respect the projectile-target symmetry which should be exact in the centre of mass of the collision. However, the backward secondaries are of little relevance and the model can be hoped to be adequate in practice.

In some models [25] an ad hoc adjustment of the above picture is made by adding a so-called "target excess" in the backward hemisphere. Here, it is not done. We prefer to leave the adjustment of the nuclear model to the last step, however at the price of being able to act on the first interactions only.

3.4.2 Nucleon-air interactions

Nucleon-air interactions are taken to be nucleon-nitrogen interactions exclusively. The volume density distribution of the nitrogen nucleus is taken of the Woods-Saxon form: $\rho=1/\{1+exp[(r-r_N)/\Delta r]\}$ with $r_N = r_{0N} 14^{1/3}$ and $\Delta r = 0.5$ fm. The incident nucleon is taken to have a cross section $log_{10}\sigma$ [mb]= $1.340+0.0642 \; log_{10} \; E_{inc}$ [GeV]. The radius r_{0N} is equal to 1.02 fm at an incident lab energy of $E_{inc}= 10^6$ GeV. In order to match the resulting nucleon nitrogen cross section with that quoted in Reference 23 a very small adjustment of the nitrogen radius has been made by having r_{0N} increases with E_{inc} [GeV] as $1.056-0.0292(log_{10}E_{inc})+0.0039 \; (log_{10}E_{inc})^2$. An interaction is described by choosing an impact parameter b at random with a uniform b^2 distribution and by calculating the number $n_{wounded}$ of nitrogen nucleons contained in the cylinder of cross section σ having as axis the incident nucleon momentum. The incident nucleon is then made to interact successively with each of the $n_{wounded}$ nucleons. The pions produced in the interactions escape the nucleus without interacting further. On the contrary, the leading nucleon re-interacts $n_{wounded} -1$ times, each time with a properly reduced energy. The nucleon nitrogen cross section is calculated as $\pi(b_{max})^2$ where b_{max} is the value of the impact parameter beyond which $n_{wounded}$ does not exceed 0.5 .

3.4.3 Iron-air interactions

An iron nucleus of incident energy E_{inc} is supposed to consist of 56 nucleons, each having an energy $E_{inc}/56$ and a momentum parallel to the incident momentum. This neglects the Fermi momentum which is of the order of the Planck constant divided by the iron radius, $\sim 200/4=50$ MeV. The distribution of nucleons inside the iron nucleus is calculated to reproduce the Woods-Saxon volume density with $r_{Fe}=1.1 \; 56^{1/3} = 4.21$ fm and $\Delta r = 0.5$ fm at incident lab energy of $E_{inc}= 10^6$ GeV. Correlations between nucleons are modelled with a hardcore interaction of radius

0.5 fm: namely, we make sure that the centres of two neighbour nucleons be never closer than $d_0 = 1$ *fm* from each other. In order to reproduce the energy dependence of the iron-nitrogen cross section given in Reference 23, the dimensions of the iron nucleus, r_{Fe} , Δr and d_0, are made to increase with energy using a scaling law of the form: $1.031 - 0.0202(log_{10}E_{inc}) + 0.0025(log_{10}E_{inc})^2$. A library of 100 such nuclei has been produced. The match between the Woods-Saxon density and that obtained here is shown in Figure 3.7. As in the case of nucleon-nitrogen interactions, an impact parameter *b* between the centres of the two interacting nuclei is chosen at random. Each of the 56 iron nucleons is then considered in sequence. In cases where it interacts with the nitrogen nucleus, the interaction proceeds as defined in the preceding paragraph. Else, the nucleon escapes freely and will interact later on with another nitrogen nucleus independently from the other nucleons of the primary iron nucleus. The inelastic interaction cross section is again calculated as $\pi(b_{max})^2$ where b_{max} is the value of the impact parameter beyond which none of the iron nucleons interacts with the nitrogen nucleus.
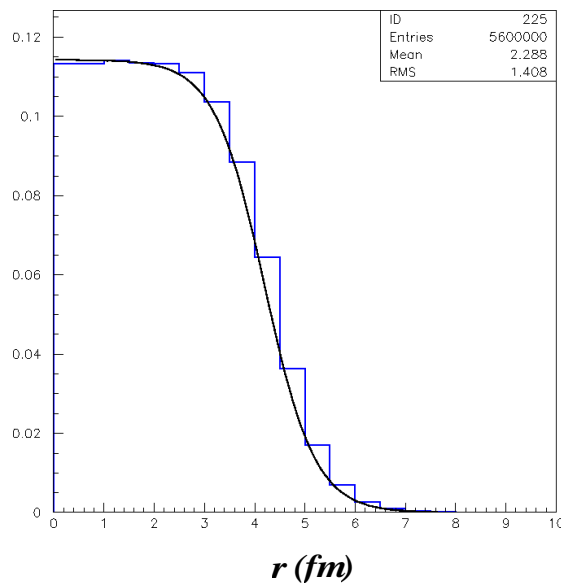
Figure 3.7: Comparison between the volume density distributions of an iron nucleus obtained from the present Monte Carlo code (histogram) and using the Wood Saxon form quoted in the text (full line).

3.4.4 Inelastic interaction cross sections

The inelastic interaction cross sections calculated as described above are compared with those used in Reference 23. As mentioned above, small adjustments have been made in order to obtain the desired energy dependence which we recall below [23]:

Nucleon nucleon: $log_{10}\sigma\,[mb] = 1.340 + 0.0642\,log_{10}\,E_{inc}\,[GeV]$

Nucleon air: $log_{10}\sigma\,[mb] = 2.332 + 0.032\,log_{10}\,E_{inc}\,[GeV]$

Iron air: $log_{10}\sigma\,[mb] = 3.197 + 0.0142\,log_{10}\,E_{inc}\,[GeV]$

The data of Reference 23 of relevance to this evaluation are reproduced below (Figure 3.8).

3.5 Charged pion decays

Neutral pions are supposed to decay promptly before interacting. Note, however, that a 1.35 EeV neutral pion has a mean decay path of 250 m. At 20 km altitude, this corresponds to 1.6 gcm^{-2} compared to a collision length of 47 gcm^{-2}.

Charged pion decays are calculated in the pion cms, where the decay muon has an isotropic distribution as shown below. Electrons from muon decays are ignored; the muons are simply removed from the set of shower particles once they have decayed.
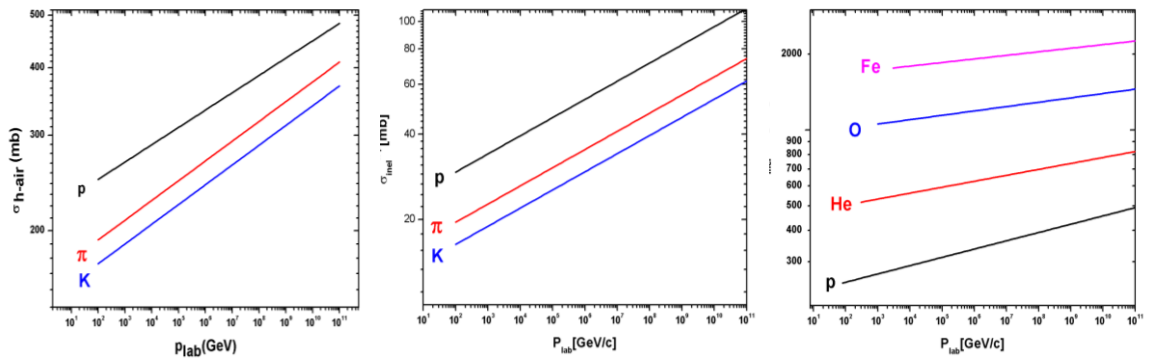
Figure 3.8: Energy dependence of inelastic cross sections as given in Reference 23. Left panel: p, π and K interacting with nucleons. Middle panel: p, π and K interacting with air. Right panel: p, He, O and Fe interacting with air.

3.5.1 Vertical incidence

For charged pion decays into muons and neutrinos, the same argument applies as for neutral pions: as the transverse momentum distribution of decay muons in the pion rest frame is invariant, the lateral scale of the lateral distribution function resulting from the decay of charged pions into muons and neutrinos is proportional to altitude above ground and inversely proportional to momentum (or energy when the pion is relativistic). Figure 3.9 shows the ground distribution of r^2, r being the distance between the muon impact on ground and that of the pion momentum, in the case of a vertical pion of 1 GeV momentum decaying at an altitude of 1 km above ground. As in the case of neutral pions, dN/dr^2 can be calculated exactly. Calling u the cosine of the angle between the pion and muon momenta in the pion rest frame, which has uniform distribution between -1 and 1, and p the muon momentum in the pion rest frame, energy conservation gives $m_\pi = p + (p^2 + m^2_\mu)^{1/2}$.

Hence, $p = \frac{1}{2}(m^2_\pi - m^2_\mu)/m_\pi = 37\ MeV/c$, and $p/m_\pi \sim \frac{1}{4}$ and $E_\mu/m_\pi = 1 - p/m_\pi \sim \frac{3}{4}$.

Writing $g = zm_\pi/E$, $r = z\tan\theta = g\sqrt{(1-u^2)}/(3+u)$. Compared with the neutral pion case (Section 2.2.1), we have 3 instead of 1 in the denominator. In the relativistic limit, $\tan\theta = \gamma - 1\sqrt{(1-u^2)}/(u+3)$ with $\gamma = E/m_\pi$, implying that $r^2 = z^2\tan^2\alpha$ contains now a factor $(1-u^2)/(3+u)^2$, which, however, does not simplify as in the neutral pion case: there is no simple analytical expression of the associated lateral distribution function.
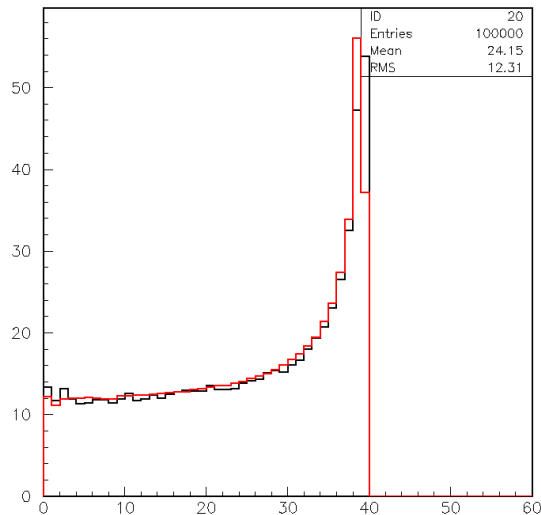
Figure 3.9: Ground distribution of r2 in the case of a vertical pion of 1 GeV momentum decaying at an altitude of 1 km above ground (black) and its analytical description (red).

This distribution is smeared by the contribution of multiple scattering, energy loss and occasional muon decays. As in the case of neutral pions with the Molière radius, this smearing breaks the simple scaling law obeyed by decay as multiple scattering depends on the quantity of matter traversed.

Figure 3.10 shows the ground distribution of r^2 for a muon having initial vertical momentum at an altitude of 10 km above ground and the energy distribution resulting from the decay of a vertical 10 GeV pion, namely ignoring decay transverse momentum. Here, r is the distance between the muon impact on ground and that of its initial momentum. The distribution results exclusively from multiple scattering, energy loss and occasional muon decays. A Gaussian fit is also shown.

Figure 3.11 shows the dependence of the variance, σ, of the above r^2 distribution, multiplied by the pion initial energy and divided by the altitude above ground as a function of the altitude above ground. Defining $\Delta z = z - z_{ground}$, the dependence takes the forms $\sigma E/\Delta z = -9.51\Delta z + 29.1\Delta z^{2/3}$ for $\Delta z \leq 10$ and $\sigma E/\Delta z = 46.25 - 0.565\Delta z$ for $\Delta z > 10$.

ID	21
Entries	159521
Mean	28.92
RMS	22.64
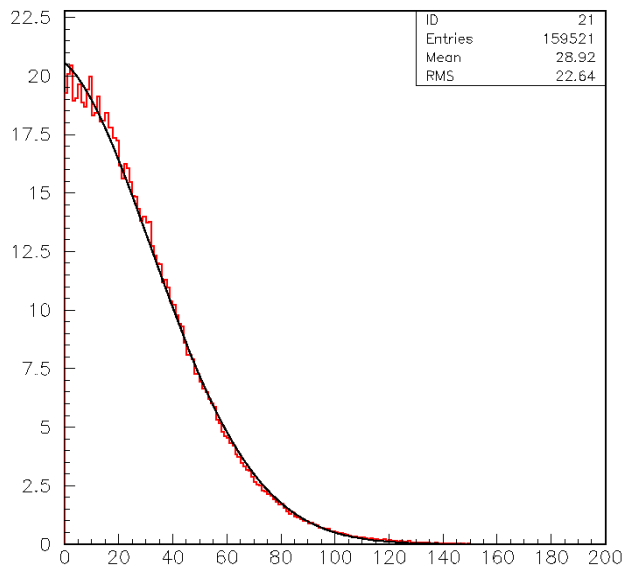
Figure 3.10: Ground distribution of r2 in the case of a vertical pion of 10 GeV momentum decaying at an altitude of 10 km above ground (red) and its Gaussian fit (black). The decay transverse momentum has been ignored (see text).
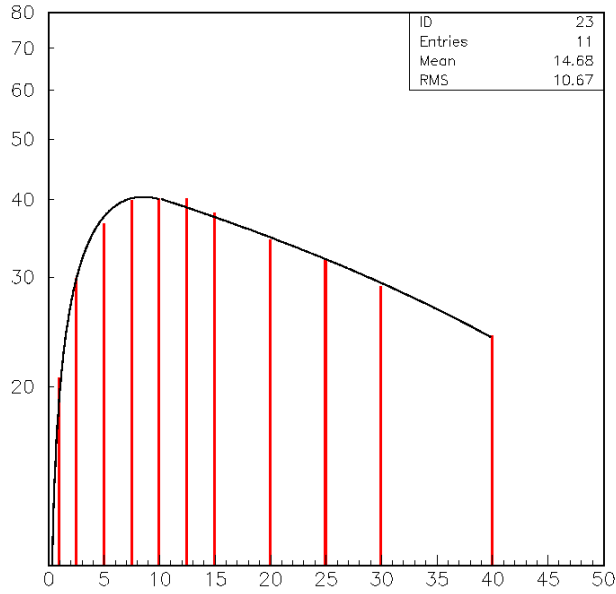
Figure 3.11: Dependence of σE/Δz as a function of Δz (see text).

3.5.2 Oblique incidence

The arguments just developed for vertical incidence apply unchanged to the case of oblique incidence as illustrated in Figures 3.12 and 3.13. Figure 3.12 shows the dependence of σ on $cos\theta$ where θ is the angle of the charged pion momentum in the case of a pion of 10 GeV momentum decaying at an altitude of 10 km above ground. It is of the form $\sigma(cos\theta)=\sigma(cos0)exp[1.75(1-cos\theta)]$. The agreement of the lateral distribution function with its parameterization is illustrated in Figure 3.13.
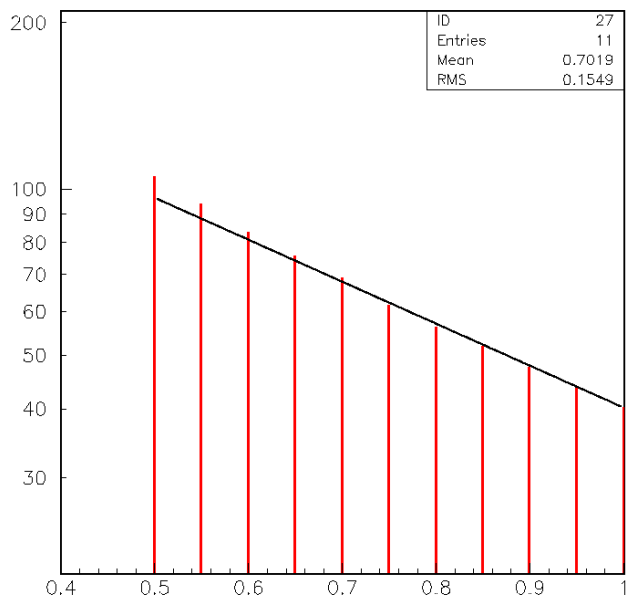
Figure 3.12: Dependence of σ on cosθ (see text).
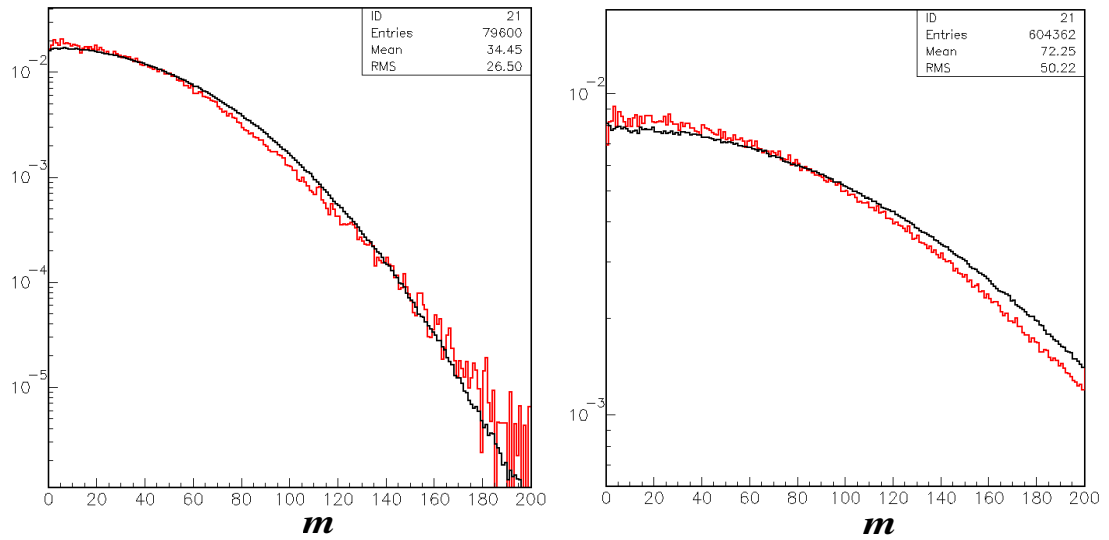
Figure 3.13: Comparison of the LDF using the parameterization described in the text (black) with the real simulation (red) in the case of a 10 GeV momentum oblique pion (cosθ =0.7) decaying at an altitude of 10 km above ground (left) or 15 km above ground (right).

4. PARAMETERISATION OF SUB-SHOWERS

4.1 General strategy

The aim is to obtain parameterisations of three profiles as a function of three variables: the profiles are the longitudinal shower profile, the muon lateral distribution function and the electron/photon lateral distribution function; the variables are associated with the primary: they are its energy, the altitude of its first interaction and the cosine of its zenith angle of incidence.

Neutral pions are made to decay into two photons that are immediately converted into parameterised sub-showers. Charged pions are made to decay or to interact according to the relative values taken by the decay length or interaction length. If they decay, they are simply converted into a muon according to the proper kinematics and using the parameterised form for the lateral distribution function. If they interact, the treatment they are given depends on the value of the ratio between their energy and the primordial energy. If this ratio is smaller than some predefined value f, say 5%, they are converted into a parameterised sub-shower. If it is larger than the predefined threshold, the hadronic interaction model describes the interaction. This procedure allows for a very rapid treatment of the shower development up to the highest energies without requiring the use of thinning or other similar methods.

It is sufficient to limit the parameterisation to pion primaries, as the only other hadrons of relevance are a very small number of nucleons. Indeed, the description of hadronic interactions used in the code does not centrally produce any nucleon (although, in reality, some nucleon-antinucleon pairs are centrally produced). Even when one starts with an iron primary, one only has 56 nucleons to start with. Each of these, when it interacts with nitrogen molecules, does not produce any new nucleon, the target nucleons being ignored as having very small energies. The primary nucleon remains the only nucleon in the interaction products, it is the leading particle, and its energy decreases by a factor at each interaction. One is then left with a maximum of, say, 1000 nucleon-induced interactions (20 interactions times 50 nucleons), which is small enough a number not to require a particular treatment. The contribution of nucleons to the development of the shower is exclusively in their ability to interact and to produce pion secondaries, which will directly contribute.

The longitudinal profile is measured (in GeV per bin of a tenth of a radiation length) along the shower axis defined as the primary momentum and extends to very large depths, well beyond ground, the assumption being that atmospheric pressure keeps increasing according to the same exponential law as in the real atmosphere. The reason is to guarantee a sensible Gaisser Hillas parameterisation of the profile, which requires performing the fit well beyond shower maximum. However, in the case of the transverse profile, the energy contained in the shower when it reaches ground, referred to as the tail energy, is fully distributed in the lateral distribution function. The charged pion and muon contributions to the longitudinal profile are ignored: we only retain that of electromagnetic showers resulting from neutral pion decays, however normalized to their energies. The lateral distribution functions are given in the plane normal to the shower axis at its intersection with ground. Obtaining the measured signal requires a projection on ground and a simulation of the detector response. The muon distribution function is given in muons per square meters and the electron/photon distribution function is given in MeV per square meters.

In a first phase, a grid is chosen in the parameter space that scans from *1 GeV* to *1 TeV*, from *cosθ=0.5* to *cosθ=1* and from *z=0* to *~22 km* above ground. Parameters are listed in Tables A1 to A3 in appendix. At each node of the grid lattice, 10000 showers are generated and the three profiles are parameterised. The parameters of a new shower are then calculated by interpolation. In practice, linear interpolations are used for *cosθ* and logarithmic interpolations for energy and altitude.

In a second phase, parameterisation is extended to higher energies stepwise, by successive iterations. In order to keep manageable computing time, showers induced by pions having energy smaller than *f* % of the primary energy are no longer simulated but simply replaced by parameterised showers. This allows extending the parameter grid up to 10^{20} eV. As a parameterised average shower replaces each sub-shower, shower-to-shower fluctuations are the exclusive result of fluctuations in the sample of interactions having incident energies exceeding *f* % of the primary energy.

Updating the longitudinal profile is done by directly adding the new sub-shower profile to the already accumulated main shower profile, starting from the depth at which the interaction occurs. However, updating the

lateral distribution functions cannot be done so simply: the sub-shower lateral distribution function is parameterized as a function of distance r_{sub} to the sub-shower axis but its contribution to the main shower must be in terms of the distance r_{main} to the main shower axis. At variance with the longitudinal case, r_{sub} and r_{main} are not related by a simple analytic form. What is done in practice is to choose 1000 values of r_{sub} at random, each with a weight of 1‰, and for each of these add the proper contribution to the r_{main} distribution.

4.2 Longitudinal profiles below 1 TeV

The parameterisation used is of the Gaisser Hillas form, $S=S_{max}\{[X-X^*]/[X_{max}-X^*]\}^{[X_{max}-X^*]/w}exp([X_{max}-X]/w)$ where S_{max} is such that the integral of the profile is the primary energy (i.e. the photon energy for the elementary photon sub-showers that make up the global profile) and X^* is the depth at which the shower starts. In practice, when adding up photon contributions, X^* is always set to zero because the new photon shower profile is added to the previously accumulated profile starting from the altitude where the photon converts rather than that where the pion decays. The same applies to the accumulated profile because it starts at the altitude where the primary pion interacts for the first time. In practice, only two parameters are required, which are simply related to the mean and rms values of the depth, as given by Relation 2.8:

$$\delta = \{<X>/Rms(X)\}^2 - 1 \qquad X_{max} = <X>\delta/(\delta+1) \qquad w = X_{max}/\delta$$

As noted in Section 2.2, $Rms(X)$, the rms value measured on the sum of 10'000 pion profiles, is not the mean value of the rms values of individual profiles. The choice made here, however, is to neglect shower-to-shower fluctuations at low energies. At low energies, the number of neutral pions produced is small, sometime even zero. It is therefore a crude approximation to accept that the longitudinal profile obtained for neutral pions applies to the whole shower. It is another crude approximation to normalize the profile to the energy carried by the primary charged pion. The only justification for such a procedure is that the simulation is meant to be used well above the TeV range where these approximations are sensible. Therefore, at each node of the grid, it is sufficient to record two parameters to define the longitudinal profile.
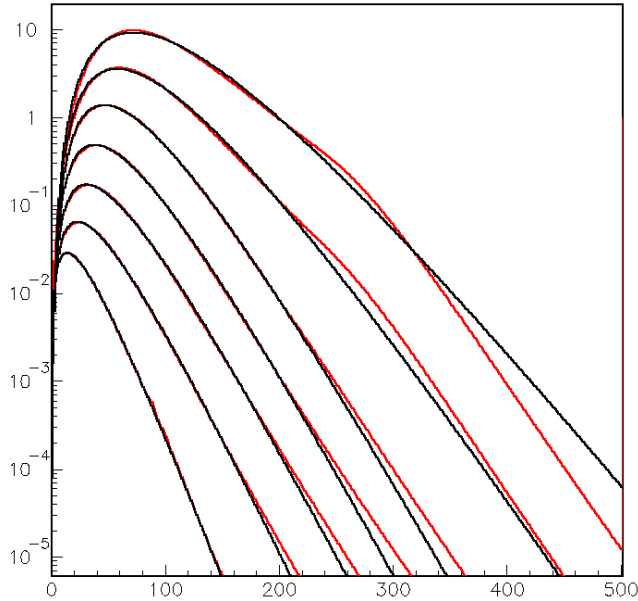
Figure 4.1: Longitudinal profiles (black) obtained for a vertical charged pion decaying at a distance of 22 km above ground for seven grid energies (1, 3.2, 10, 32,100, 320 and 1000 GeV). The lines show the result of the Gaisser Hillas parameterisation. Depths (abscissa) are in bins of a tenth of a radiation length and ordinate in GeV/bin.

Finally, we recall that the longitudinal profile is evaluated by projection on the shower axis, defined by the primary momentum. The results of the parameterisation are listed in Table A1 and illustrated in Figure 4.1.

4.3 Electron/photon lateral distribution functions below 1TeV

The parameterisation used is of the form $exp\{a+b(lnr)^c\}$ with the distance r measured in meters and the lateral distribution function evaluated in MeV per square meter. At low energies it sometimes happens that the energy reaching ground is negligible and a sensible parameterisation cannot be directly produced. In such cases, the parameterisation is simply scaled down from that obtained at the higher energy node of the grid. As mentioned earlier, the distance r is measured from the intersection with ground of the momentum of the primary in the plane normal to this momentum. The results of the parameterisation are listed in Table A2 and illustrated in Figure 4.2
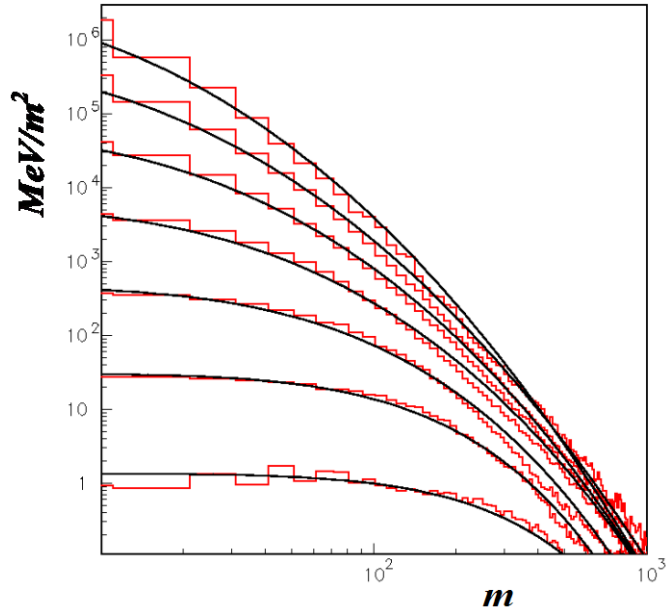
Figure 4.2: Electron/photon lateral distribution functions obtained for a vertical charged pion decaying at a distance of 1 km above ground for seven grid energies (1, 3.2, 10, 32,100, 320 and 1000 GeV). The lines show the parameterisation. Distances (abscissa) are in m and the ordinate, in MeV/m^2, is integrated over 10000 showers.

4.4 Muon lateral distribution functions below 1TeV

The parameterisation used is of the form *exp{a+b(lnr)^c}* with the distance *r* measured in meters and the lateral distribution function evaluated in muons per square meter. At low energies (essentially 1 GeV) it sometimes happens that so few muons reach ground that a sensible parameterisation cannot be directly produced. In such cases, the parameterisation is simply scaled down from that obtained at the higher energy node of the grid. As mentioned earlier, the distance *r* is measured from the intersection with ground of the momentum of the primary in the plane normal to this momentum. At each node of the grid, 10000 showers are generated. Figure 4.3 illustrates the kind of results that are obtained, using as an example the case of a vertical muon decaying at an altitude of 1 km above ground. The results of the parameterisation are listed in Table A3.
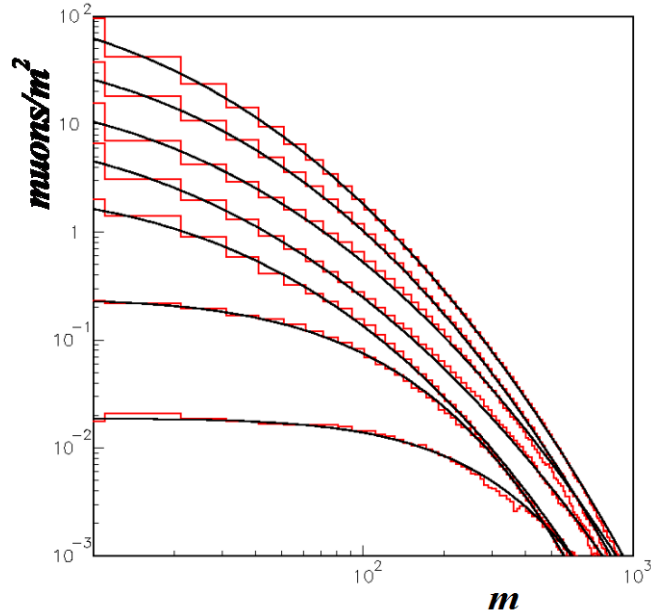
Figure 4.3 Muon lateral distribution functions obtained for a vertical charged pion decaying at a distance of 1 km above ground for seven grid energies (1, 3.2, 10, 32,100, 320 and 1000 GeV). The lines show the parameterisation. Distances (abscissa) are in m and ordinate (in muons/m^2) is integrated over 10000 showers.

4.5 Parameterisations from 1 TeV to 0.1 ZeV

Going up in energy still implies recording parameters that describe, at each node of the grid, the longitudinal profile and the lateral distribution functions. The difference with what was done below 1 TeV is that each interacting charged pion having energy lower than 5 % of the primary charged pion energy is now replaced by a parameterised sub-shower. This is done by interpolation between the values taken by the parameters in the relevant region of the grid. The technique used for the lateral distribution functions is the same as described in the last paragraph of Section 4.1.

We recall that in the case of photons, whatever their energy, we replace them by sub-showers having Gaussian shower-to-shower fluctuations rather than by fixed average sub-showers. This is done by retaining, for each node of the grid, the values of *<<X>>, Rms(<X>), <ρ> and Rms(ρ)* as was done previously in Section 2 (see Figure 2.4).

For the interpolation to work properly in the case of the lateral distribution functions, we noted that it should be made on a parameter $b'=b\{ln(400)\}^c$ rather than on b, the former being much better behaved than the latter and much less correlated with c. Moreover, interpolation must now be made on z rather than on $z-z_{ground}$ in order to avoid divergences

near ground. Finally, on the low-energy-, low-altitude- and high-altitude-edges of the grid, extrapolation outside the grid range is made on *a* exclusively, *b* and *c* being fixed at the values they have on the edge of the grid. Moreover, in the case of low energies, when such extrapolation requires going beyond a grid cell, the lateral distribution function is simply set to zero.

In the case of the longitudinal profile, we recall that we continue the shower development below ground in order not to bias the parameterisation of the profile (which, however, is only used above ground). However, this implies that we need to account for the possible presence of charged pions reaching ground with some significant energy. Neglecting them or simply making them deposit their energy on ground would bias the profile to shorter depths. What is done, therefore, is to replace them by neutral pions as soon as they reach ground and add to the profile the corresponding contribution properly weighted. As, in practice, only low energy charged pions actually reach ground, this approximation is acceptable.

Figures 4.4 to 4.6 display the lateral distribution functions and longitudinal profiles obtained for a vertical charged pion converting 22 km above ground for energies in geometrical progression between 10 TeV and 0.1 ZeV.
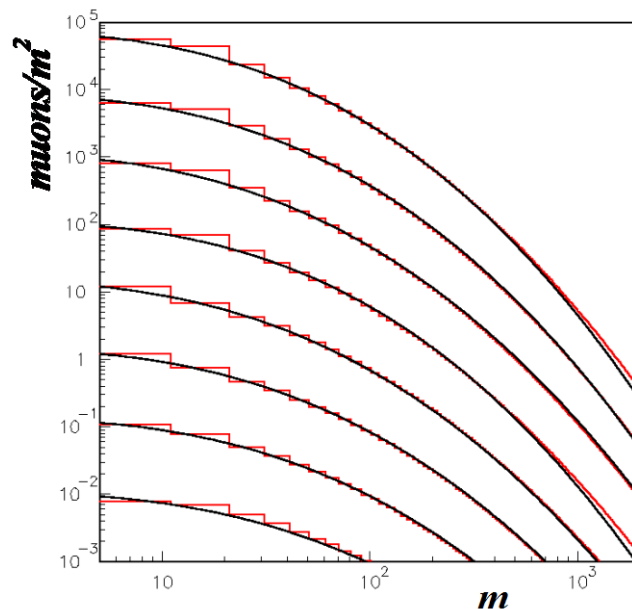
Figure 4.4. Muon lateral distribution functions obtained for primary vertical charged pions of energies in geometric progression from 10 TeV to 0.1 ZeV and interacting at 22 km above ground. The units are metres in abscissa and muons per m2 in ordinate.
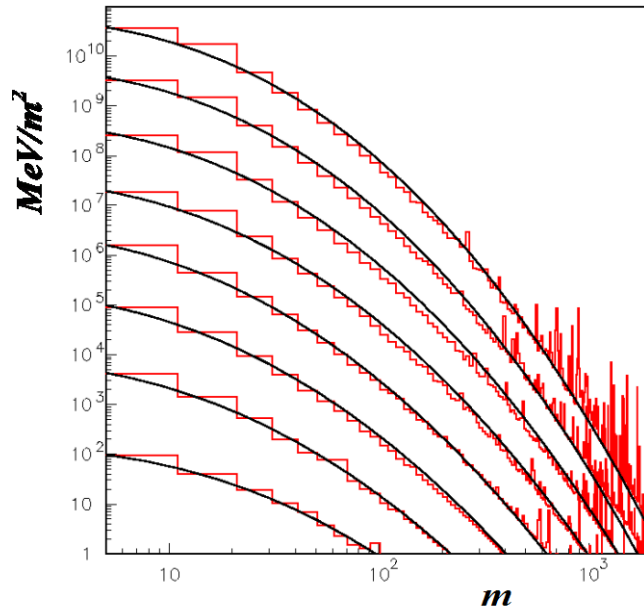
Figure 4.5. Electron/photon distribution functions obtained for primary vertical charged pions of energies in geometric progression from 10 TeV to 0.1 ZeV and interacting at 22 km above ground. The units are metres in abscissa and MeV/m2 in ordinate.
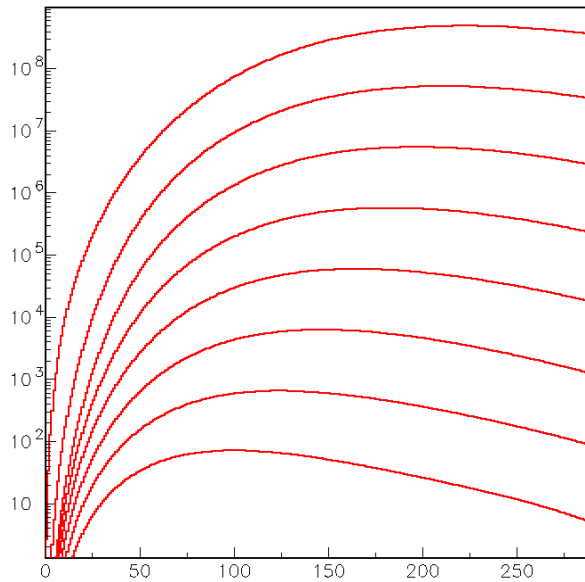
Figure 4.6. Longitudinal profiles obtained for primary vertical charged pions of energies in geometric progression from 10 TeV to 0.1 ZeV and interacting at 23.4 km a.s.l. The unit of abscissa is 0.1 radiation length, that of ordinate is such that the integral of the profile is the primary energy. The abscissa stops at sea level (29.0 radiation lengths).

4.6 Proton-iron discrimination

As an illustration of the performance of the simulation, we consider its prediction in the UHECR regime for proton and iron primaries separately. Figure 4.7 shows the result obtained for the longitudinal profile. Both $<X_{max}>$ and $Rms(X_{max})$ are seen to be consistent with the predictions of more sophisticated codes. It is a remarkable result in view of the crudeness of some of the approximations made in the present model. Figure 4.8 shows the muon lateral distribution functions at 1 and 10 EeV for protons and iron separately. Their ratio is found to be 1.33, in excellent agreement with the prediction, 1.32, of other simulation codes (see Figure 1.16). The electron-photon lateral distribution function is not directly accessible to experiment: the measured distribution is a weighted sum of the muon and electron-photon distributions, each including the corresponding detector response. In particular in the UHECR regime, where the distance of relevance is very large (1km in the Pierre Auger case), the resulting distribution is strongly detector dependent.
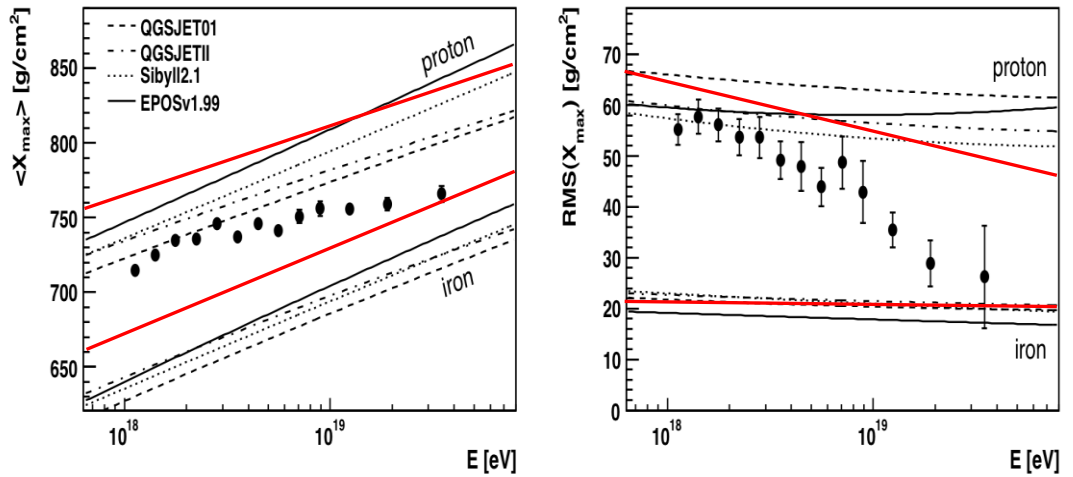
Figure 4.7: $<X_{max}>$ and $RMS(X_{max})$ compared with air shower simulations using different hadronic interaction models.
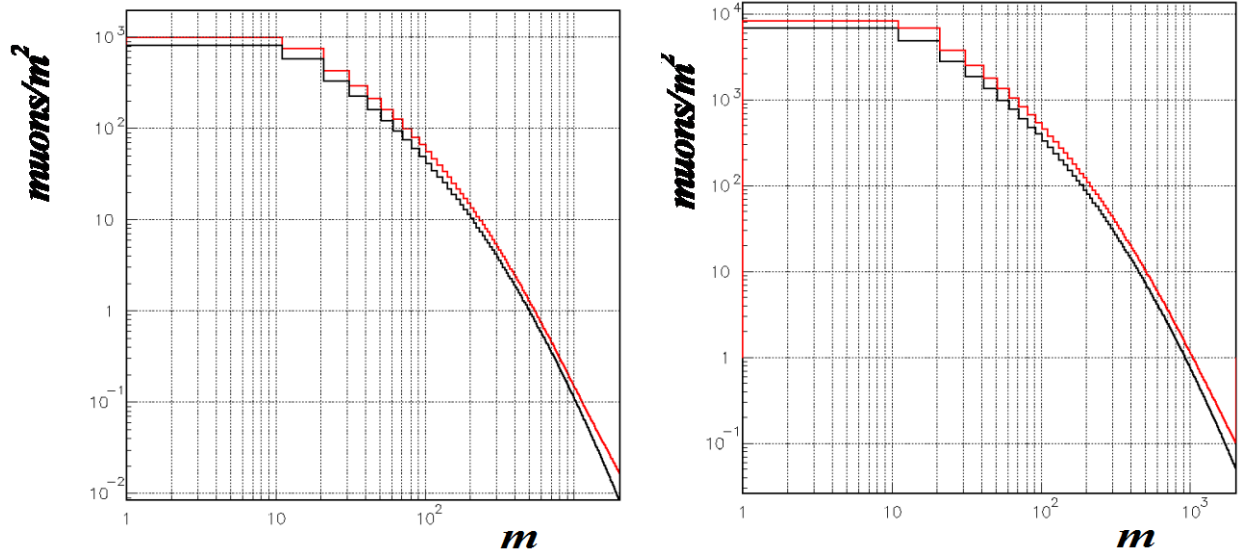
Figure 4.8: The muon lateral distribution functions at 1 EeV(left) and 10 EeV (right) for proton(black) and iron(red).

5. SUMMARY AND CONCLUSIONS

We have conceived and written a computer code that simulates the development of extensive air showers up to extreme energies. The originality of our approach, flexibility, transparency and rapidity, are at the price of major simplifications and approximations in the underlying physics. Yet, its interest as a complement to existing sophisticated codes has been amply demonstrated with the simple illustrating example of iron-proton discrimination.

The cases of electromagnetic and hadronic showers have been treated separately. The former is much simpler in many respects: the shower development depends exclusively of the depth traversed, in g/cm^2, which considerably eases the parameterization of the longitudinal and transverse profiles. On the contrary, the latter depends on two scales: the interaction length, in g/cm^2, governs interactions while the decay length, in meters, governs decays. As both processes, interactions and decays, are in competition, the nice scaling properties of electromagnetic showers no longer apply in the case of hadronic showers. To face this difficulty, we have used a three-dimensional grid in energy, altitude and obliquity, at the nodes of which we have evaluated the parameters that describe the longitudinal and transverse profiles. Interpolation between the nodes of the grid provides the parameterization at any point in the three-dimensional space.

The method consists in following the details of the shower development for high energy charged secondaries exclusively. All neutral pions and charged pions having an energy smaller than a given fraction of the primary energy are described as parameterised sub-showers using the parameter grid mentioned above. However, in the case of neutral pions having an energy smaller than the mentioned fraction of the primary energy, the parameterised forms are made to fluctuate around their mean with Gaussian deviations. The gain in computer time is considerable. The shower-to-shower fluctuations are nevertheless properly reproduced as are the differences between iron-induced and proton-induced showers, because, in both cases, they are determined by the first interactions exclusively.

In practice, the description of the profiles has been limited to only three distributions: the longitudinal profile (essentially made of its electron/photon component), the electron/photon lateral distribution function and the muon lateral distribution function. Simple forms (Gaisser

Hillas for the longitudinal profile and $exp\{a+b(lnr)^c\}$ for the lateral distribution functions) have been found adequate. While these are sufficient for a large number of problems, additional information would sometimes be useful: examples are the distribution of the times of arrival of secondaries on ground and the distribution of the altitudes where the muons reaching ground have been produced. Such improvements would be valuable upgrades of the existing codes and should be implemented as soon as sufficient experience will have been gained with the present code.

6. ANNEX

Table A1:Parameters of the longitudinal profile using a Gaisser Hillas form

$$S=S_{max}\{X/X_{max}\}^{Xmax/w}exp([X_{max}-X]/w) \text{ where } \rho=Rms(X)/<X>$$

Energy (GeV)	Altitude (km)	$cos\theta$	Mean $<X>-X_0$	Mean ρ (%)
1	1	1	2.35	64.5
1	2.2	1	2.55	67.5
1	4.6	1	2.55	68.5
1	10	1	2.55	69.5
1	22	1	2.55	69.5
3	1	1	3.45	61.5
3	2.2	1	3.65	61.5
3	4.6	1	3.75	62.5
3	10	1	3.75	62.5
3	22	1	3.75	62.5
10	1	1	4.45	57.5
10	2.2	1	4.65	57.5
10	4.6	1	4.65	58.5
10	10	1	4.65	58.5
10	22	1	4.65	58.5
32	1	1	5.25	53.5
32	2.2	1	5.65	53.5
32	4.6	1	5.65	54.5
32	10	1	5.45	54.5
32	22	1	5.45	54.5
100	1	1	6.05	50.5
100	2.2	1	6.65	49.5
100	4.6	1	6.95	51.5
100	10	1	6.75	52.5
100	22	1	6.35	51.5
320	1	1	6.85	47.5
320	2.2	1	7.55	46.5
320	4.6	1	8.25	48.5
320	10	1	8.35	51.5
320	22	1	7.75	51.5
1000	1	1	7.85	45.5
1000	2.2	1	8.55	43.5
1000	4.6	1	9.45	45.5
1000	10	1	9.85	48.5
1000	22	1	9.55	50.5

Energy (GeV)	Altitude (km)	$cos\theta$	Mean $<X>-X_0$	Mean ρ (%)
1	1	0.9	2.45	65.5
1	2.2	0.9	2.55	68.5
1	4.6	0.9	2.65	68.5
1	10	0.9	2.65	69.5
1	22	0.9	2.65	69.5
3	1	0.9	3.55	61.5
3	2.2	0.9	3.75	62.5
3	4.6	0.9	3.75	62.5
3	10	0.9	3.75	62.5
3	22	0.9	3.75	63.5
10	1	0.9	4.45	56.5
10	2.2	0.9	4.75	57.5
10	4.6	0.9	4.75	58.5
10	10	0.9	4.65	57.5
10	22	0.9	4.65	58.5
32	1	0.9	5.25	53.5
32	2.2	0.9	5.65	53.5
32	4.6	0.9	5.65	54.5
32	10	0.9	5.45	54.5
32	22	0.9	5.45	54.5
100	1	0.9	6.15	49.5
100	2.2	0.9	6.75	49.5
100	4.6	0.9	6.95	52.5
100	10	0.9	6.75	52.5
100	22	0.9	6.25	51.5
320	1	0.9	6.95	47.5
320	2.2	0.9	7.75	46.5
320	4.6	0.9	8.35	48.5
320	10	0.9	8.25	51.5
320	22	0.9	7.75	51.5
1000	1	0.9	7.95	45.5
1000	2.2	0.9	8.75	43.5
1000	4.6	0.9	9.65	45.5
1000	10	0.9	9.85	49.5
1000	22	0.9	9.55	50.5

Energy (GeV)	Altitude (km)	$cos\theta$	Mean $<X>-X_0$	Mean ρ (%)
1	1	0.8	2.45	66.5
1	2.2	0.8	2.65	68.5
1	4.6	0.8	2.65	68.5
1	10	0.8	2.65	69.5
1	22	0.8	2.65	70.5
3	1	0.8	3.55	61.5
3	2.2	0.8	3.75	62.5
3	4.6	0.8	3.75	62.5
3	10	0.8	3.75	63.5
3	22	0.8	3.75	63.5
10	1	0.8	4.55	56.5
10	2.2	0.8	4.75	57.5
10	4.6	0.8	4.75	58.5
10	10	0.8	4.75	58.5
10	22	0.8	4.65	58.5
32	1	0.8	5.35	52.5
32	2.2	0.8	5.75	53.5
32	4.6	0.8	5.65	54.5
32	10	0.8	5.45	54.5
32	22	0.8	5.45	54.5
100	1	0.8	6.25	49.5
100	2.2	0.8	6.85	49.5
100	4.6	0.8	6.95	52.5
100	10	0.8	6.75	52.5
100	22	0.8	6.35	51.5
320	1	0.8	7.05	46.5
320	2.2	0.8	7.95	46.5
320	4.6	0.8	8.45	49.5
320	10	0.8	8.25	52.5
320	22	0.8	7.75	51.5
1000	1	0.8	8.05	44.5
1000	2.2	0.8	8.95	43.5
1000	4.6	0.8	9.75	46.5
1000	10	0.8	9.95	50.5
1000	22	0.8	9.55	50.5

Energy (GeV)	Altitude (km)	$cos\theta$	Mean $<X>-X_0$	Mean ρ (%)
1	1	0.7	2.55	66.5
1	2.2	0.7	2.65	67.5
1	4.6	0.7	2.65	68.5
1	10	0.7	2.65	68.5
1	22	0.7	2.65	71.5
3	1	0.7	3.65	61.5
3	2.2	0.7	3.75	62.5
3	4.6	0.7	3.75	62.5
3	10	0.7	3.75	62.5
3	22	0.7	3.75	63.5
10	1	0.7	4.65	56.5
10	2.2	0.7	4.75	57.5
10	4.6	0.7	4.75	57.5
10	10	0.7	4.75	58.5
10	22	0.7	4.65	58.5
32	1	0.7	5.55	52.5
32	2.2	0.7	5.75	53.5
32	4.6	0.7	5.75	54.5
32	10	0.7	5.55	54.5
32	22	0.7	5.45	54.5
100	1	0.7	6.35	48.5
100	2.2	0.7	6.95	49.5
100	4.6	0.7	7.05	52.5
100	10	0.7	6.65	52.5
100	22	0.7	6.25	51.5
320	1	0.7	7.25	46.5
320	2.2	0.7	8.15	46.5
320	4.6	0.7	8.65	50.5
320	10	0.7	8.35	52.5
320	22	0.7	7.55	50.5
1000	1	0.7	8.15	44.5
1000	2.2	0.7	9.15	43.5
1000	4.6	0.7	10.05	47.5
1000	10	0.7	9.95	51.5
1000	22	0.7	9.55	50.5

Energy (GeV)	Altitude (km)	$cos\theta$	Mean $<X>-X_0$	Mean ρ (%)
1	1	0.6	2.55	67.5
1	2.2	0.6	2.65	67.5
1	4.6	0.6	2.65	68.5
1	10	0.6	2.65	68.5
1	22	0.6	2.65	72.5
3	1	0.6	3.75	61.5
3	2.2	0.6	3.75	62.5
3	4.6	0.6	3.75	62.5
3	10	0.6	3.75	62.5
3	22	0.6	3.75	63.5
10	1	0.6	4.75	55.5
10	2.2	0.6	4.75	56.5
10	4.6	0.6	4.75	57.5
10	10	0.6	4.75	58.5
10	22	0.6	4.75	58.5
32	1	0.6	5.65	51.5
32	2.2	0.6	5.85	53.5
32	4.6	0.6	5.75	53.5
32	10	0.6	5.55	53.5
32	22	0.6	5.45	54.5
100	1	0.6	6.55	48.5
100	2.2	0.6	7.15	50.5
100	4.6	0.6	7.15	52.5
100	10	0.6	6.65	52.5
100	22	0.6	6.25	51.5
320	1	0.6	7.45	45.5
320	2.2	0.6	8.35	47.5
320	4.6	0.6	8.75	51.5
320	10	0.6	8.25	52.5
320	22	0.6	7.55	50.5
1000	1	0.6	8.45	43.5
1000	2.2	0.6	9.45	43.5
1000	4.6	0.6	10.25	48.5
1000	10	0.6	10.05	51.5
1000	22	0.6	9.35	50.5

Energy (GeV)	Altitude (km)	$cos\theta$	Mean $<X>-X_0$	Mean ρ (%)
1	1	0.5	2.55	67.5
1	2.2	0.5	2.75	68.5
1	4.6	0.5	2.65	68.5
1	10	0.5	2.65	69.5
1	22	0.5	2.65	71.5
3	1	0.5	3.75	61.5
3	2.2	0.5	3.85	62.5
3	4.6	0.5	3.75	62.5
3	10	0.5	3.75	63.5
3	22	0.5	3.85	64.5
10	1	0.5	4.85	55.5
10	2.2	0.5	4.85	56.5
10	4.6	0.5	4.75	57.5
10	10	0.5	4.75	57.5
10	22	0.5	4.75	58.5
32	1	0.5	5.85	51.5
32	2.2	0.5	5.95	53.5
32	4.6	0.5	5.75	53.5
32	10	0.5	5.55	53.5
32	22	0.5	5.45	54.5
100	1	0.5	6.75	48.5
100	2.2	0.5	7.35	51.5
100	4.6	0.5	7.15	52.5
100	10	0.5	6.65	51.5
100	22	0.5	6.35	51.5
320	1	0.5	7.75	45.5
320	2.2	0.5	8.65	47.5
320	4.6	0.5	8.85	52.5
320	10	0.5	8.25	52.5
320	22	0.5	7.55	49.5
1000	1	0.5	8.75	42.5
1000	2.2	0.5	9.95	44.5
1000	4.6	0.5	10.45	50.5
1000	10	0.5	10.05	51.5
1000	22	0.5	9.25	50.5

Table A2: Parameters of the electron/photon lateral distribution function (MeV/m^2) using a form $exp\{a+b(lnr)^c\}$ with the distance r measured in meters

Energy (GeV)	Altitude (km)	cosθ	a	b	c
1	1	1	−8.92E+00	−5.90E−06	7.10E+00
1	2	1	−1.26E+01	−2.86E−07	8.31E+00
1	5	1	0.00E+00	0.00E+00	0.00E+00
1	10	1	0.00E+00	0.00E+00	0.00E+00
1	22	1	0.00E+00	0.00E+00	0.00E+00
3.2	1	1	−5.80E+00	−1.13E−04	5.80E+00
3.2	2	1	−8.55E+00	−7.96E−06	6.90E+00
3.2	5	1	−1.32E+01	−6.07E−07	7.90E+00
3.2	10	1	0.00E+00	0.00E+00	0.00E+00
3.2	22	1	0.00E+00	0.00E+00	0.00E+00
10	1	1	−3.09E+00	−3.02E−03	4.20E+00
10	2	1	−5.53E+00	−3.34E−04	5.14E+00
10	5	1	−9.06E+00	−2.23E−04	5.16E+00
10	10	1	−1.46E+01	−9.81E−04	4.16E+00
10	22	1	0.00E+00	0.00E+00	0.00E+00
32	1	1	−5.78E−01	−1.96E−02	3.30E+00
32	2	1	−2.46E+00	−3.49E−03	4.10E+00
32	5	1	−5.48E+00	−1.48E−03	4.40E+00
32	10	1	−1.05E+01	−2.61E−04	5.10E+00
32	22	1	0.00E+00	0.00E+00	0.00E+00
100	1	1	1.73E+00	−5.08E−02	2.90E+00
100	2	1	5.10E+00	−2.07E−02	3.30E+00
100	5	1	−2.02E+00	−9.18E−03	3.60E+00
100	10	1	−5.57E+00	−7.41E−03	3.60E+00
100	22	1	−9.79E+00	−2.22E−03	4.10E+00
320	1	1	3.98E+00	−1.24E−01	2.50E+00
320	2	1	3.09E+00	−7.40E−02	2.70E+00
320	5	1	1.25E+00	−4.36E−02	2.90E+00
320	10	1	−1.38E+00	−2.20E−02	3.20E+00
320	22	1	−3.57E+00	−1.70E−02	3.30E+00
1000	1	1	5.78E+00	−1.72E−01	2.40E+00
1000	2	1	5.32E+00	−1.47E−01	2.40E+00
1000	5	1	3.94E+00	−9.31E−02	2.60E+00
1000	10	1	1.84E+00	−5.74E−02	2.80E+00
1000	22	1	−3.12E−01	−2.52E−02	3.20E+00

Energy (GeV)	Altitude (km)	cosθ	a	b	c
1	1	1	−9.27E+00	−2.43E−07	8.80E+00
1	2	1	−1.34E+01	−3.80E−10	1.16E+01
1	5	1	0.00E+00	0.00E+00	0.00E+00
1	10	1	0.00E+00	0.00E+00	0.00E+00
1	22	1	0.00E+00	0.00E+00	0.00E+00
3.2	1	1	−6.11E+00	−8.65E−05	5.90E+00
3.2	2	1	−8.91E+00	−5.00E−05	5.90E+00
3.2	5	1	−1.47E+01	−2.22E−07	8.30E+00
3.2	10	1	0.00E+00	0.00E+00	0.00E+00
3.2	22	1	0.00E+00	0.00E+00	0.00E+00
10	1	1	−3.27E+00	−2.41E−03	4.30E+00
10	2	1	−5.94E+00	−3.11E−04	5.15E+00
10	5	1	−1.00E+01	−1.03E−04	5.50E+00
10	10	1	0.00E+00	0.00E+00	0.00E+00
10	22	1	0.00E+00	0.00E+00	0.00E+00
32	1	1	−7.43E−01	−1.36E−02	3.50E+00
32	2	1	−2.75E+00	−3.40E−03	4.10E+00
32	5	1	−6.52E+00	−9.12E−04	4.60E+00
32	10	1	−1.18E+01	−2.65E−04	5.10E+00
32	22	1	0.00E+00	0.00E+00	0.00E+00
100	1	1	1.64E+00	−4.95E−02	2.90E+00
100	2	1	1.60E−01	−1.94E−02	3.30E+00
100	5	1	−2.56E+00	−7.48E−03	3.70E+00
100	10	1	−6.70E+00	−3.20E−03	4.05E+00
100	22	1	−1.17E+01	−1.14E−04	5.60E+00
320	1	1	3.84E+00	−1.03E−01	2.60E+00
320	2	1	2.92E+00	−7.24E−02	2.70E+00
320	5	1	7.69E−01	−3.53E−02	3.00E+00
320	10	1	−1.83E+00	−2.68E−02	3.10E+00
320	22	1	−4.47E+00	−2.12E−02	3.20E+00
1000	1	1	5.84E+00	−1.98E−01	2.30E+00
1000	2	1	5.16E+00	−1.34E−01	2.45E+00
1000	5	1	3.69E+00	−1.06E−01	2.50E+00
1000	10	1	1.01E+00	−4.50E−02	2.90E+00
1000	22	1	−1.13E+00	−2.09E−02	3.30E+00

Energy (GeV)	Altitude (km)	cosθ	a	b	c
1	1	1	−1.06E+01	−1.81E−10	1.23E+01
1	2	1	−1.41E+01	−2.33E−06	7.07E+00
1	5	1	0.00E+00	0.00E+00	0.00E+00
1	10	1	0.00E+00	0.00E+00	0.00E+00
1	22	1	0.00E+00	0.00E+00	0.00E+00
3.2	1	1	−6.37E+00	−1.14E−04	5.72E+00
3.2	2	1	−9.77E+00	−1.28E−06	7.74E+00
3.2	5	1	−1.67E+01	−8.22E−06	6.30E+00
3.2	10	1	0.00E+00	0.00E+00	0.00E+00
3.2	22	1	0.00E+00	0.00E+00	0.00E+00
10	1	1	−3.54E+00	−2.29E−03	4.30E+00
10	2	1	−6.26E+00	−6.02E−04	4.80E+00
10	5	1	−1.16E+01	−5.95E−05	5.70E+00
10	10	1	0.00E+00	0.00E+00	0.00E+00
10	22	1	0.00E+00	0.00E+00	0.00E+00
32	1	1	−1.07E+00	−1.47E−02	3.40E+00
32	2	1	−3.27E+00	−2.64E−03	4.20E+00
32	5	1	−7.54E+00	−4.80E−04	4.90E+00
32	10	1	−1.40E+01	−3.05E−04	4.90E+00
32	22	1	0.00E+00	0.00E+00	0.00E+00
100	1	1	1.51E+00	−4.78E−02	2.90E+00
100	2	1	−1.20E−01	−2.22E−02	3.20E+00
100	5	1	−3.02E+00	−1.06E−02	3.50E+00
100	10	1	−7.61E+00	−6.21E−03	3.70E+00
100	22	1	0.00E+00	0.00E+00	0.00E+00
320	1	1	3.75E+00	−1.00E−01	2.60E+00
320	2	1	2.64E+00	−6.97E−02	2.70E+00
320	5	1	2.99E−01	−3.43E−02	3.00E+00
320	10	1	−3.02E+00	−1.42E−02	3.40E+00
320	22	1	−6.27E+00	−8.99E−03	3.60E+00
1000	1	1	5.82E+00	−1.95E−01	2.30E+00
1000	2	1	5.00E+00	−1.41E−01	2.40E+00
1000	5	1	3.16E+00	−8.71E−02	2.60E+00
1000	10	1	5.22E−01	−5.36E−02	2.80E+00
1000	22	1	−1.70E+00	−5.46E−02	2.80E+00

Energy (GeV)	Altitude (km)	cosθ	a	b	c
1	1	1	−1.04E+01	−2.96E−06	7.23E+00
1	2	1	−1.55E+01	−1.13E−06	7.21E+00
1	5	1	0.00E+00	0.00E+00	0.00E+00
1	10	1	0.00E+00	0.00E+00	0.00E+00
1	22	1	0.00E+00	0.00E+00	0.00E+00
3.2	1	1	−6.74E+00	−6.19E−05	6.01E+00
3.2	2	1	−1.09E+01	−2.03E−07	8.56E+00
3.2	5	1	0.00E+00	0.00E+00	0.00E+00
3.2	10	1	0.00E+00	0.00E+00	0.00E+00
3.2	22	1	0.00E+00	0.00E+00	0.00E+00
10	1	1	−4.12E+00	−5.83E−04	5.00E+00
10	2	1	−7.33E+00	−7.75E−05	5.80E+00
10	5	1	−1.33E+01	−4.20E−06	6.94E+00
10	10	1	0.00E+00	0.00E+00	0.00E+00
10	22	1	0.00E+00	0.00E+00	0.00E+00
32	1	1	−1.23E+00	−1.04E−02	3.60E+00
32	2	1	−3.87E+00	−2.07E−03	4.30E+00
32	5	1	−8.88E+00	−4.28E−04	4.90E+00
32	10	1	0.00E+00	0.00E+00	0.00E+00
32	22	1	0.00E+00	0.00E+00	0.00E+00
100	1	1	1.20E+00	−3.25E−02	3.10E+00
100	2	1	−5.40E−01	−1.81E−02	3.30E+00
100	5	1	−3.98E+00	−8.29E−03	3.60E+00
100	10	1	−1.25E+01	−3.08E−06	7.37E+00
100	22	1	0.00E+00	0.00E+00	0.00E+00
320	1	1	3.62E+00	−9.63E−02	2.60E+00
320	2	1	2.32E+00	−6.72E−02	2.70E+00
320	5	1	−3.15E−01	−3.93E−02	2.90E+00
320	10	1	−4.11E+00	−1.65E−02	3.30E+00
320	22	1	−1.05E+01	−5.95E−04	4.90E+00
1000	1	1	5.59E+00	−1.58E−01	2.40E+00
1000	2	1	4.61E+00	−1.06E−01	2.55E+00
1000	5	1	2.41E+00	−8.06E−02	2.60E+00
1000	10	1	−1.17E+00	−2.69E−02	3.10E+00
1000	22	1	−3.23E+00	−3.81E−02	3.00E+00

Energy (GeV)	Altitude (km)	cosθ	a	b	c
1	1	1	–1.16E+01	–3.05E–06	7.01E+00
1	2	1	–1.63E+01	–3.02E–07	7.82E+00
1	5	1	0.00E+00	0.00E+00	0.00E+00
1	10	1	0.00E+00	0.00E+00	0.00E+00
1	22	1	0.00E+00	0.00E+00	0.00E+00
3.2	1	1	–7.48E+00	–5.70E–05	5.95E+00
3.2	2	1	–1.19E+01	–1.17E–06	7.59E+00
3.2	5	1	0.00E+00	0.00E+00	0.00E+00
3.2	10	1	0.00E+00	0.00E+00	0.00E+00
3.2	22	1	0.00E+00	0.00E+00	0.00E+00
10	1	1	–4.52E+00	–5.47E–04	5.00E+00
10	2	1	–8.26E+00	–1.75E–04	5.30E+00
10	5	1	–1.46E+01	–1.31E–04	5.30E+00
10	10	1	0.00E+00	0.00E+00	0.00E+00
10	22	1	0.00E+00	0.00E+00	0.00E+00
32	1	1	–1.66E+00	–9.46E–03	3.60E+00
32	2	1	–4.78E+00	–1.83E–03	4.30E+00
32	5	1	–1.00E+01	–5.99E–04	4.80E+00
32	10	1	0.00E+00	0.00E+00	0.00E+00
32	22	1	0.00E+00	0.00E+00	0.00E+00
100	1	1	1.03E+00	–3.15E–02	3.10E+00
100	2	1	–1.14E+00	–1.69E–02	3.30E+00
100	5	1	–5.16E+00	–6.58E–03	3.70E+00
100	10	1	–1.38E+01	–4.24E–04	4.90E+00
100	22	1	0.00E+00	0.00E+00	0.00E+00
320	1	1	3.39E+00	–7.92E–02	2.70E+00
320	2	1	1.88E+00	–5.57E–02	2.80E+00
320	5	1	–1.12E+00	–3.82E–02	2.90E+00
320	10	1	–5.13E+00	–2.69E–02	3.05E+00
320	22	1	–9.59E+00	–1.73E–02	3.45E+00
1000	1	1	5.55E+00	–1.56E–01	2.40E+00
1000	2	1	4.26E+00	–1.10E–01	2.50E+00
1000	5	1	1.96E+00	–9.73E–02	2.50E+00
1000	10	1	–1.57E+00	–5.09E–02	2.80E+00
1000	22	1	–4.65E+00	–3.60E–04	5.76E+00

Energy (GeV)	Altitude (km)	cosθ	a	b	c
1	1	1	–1.24E+01	–3.18E–07	8.04E+00
1	2	1	–1.70E+01	–3.18E–07	8.04E+00
1	5	1	0.00E+00	0.00E+00	0.00E+00
1	10	1	0.00E+00	0.00E+00	0.00E+00
1	22	1	0.00E+00	0.00E+00	0.00E+00
3.2	1	1	–8.36E+00	–5.67E–06	7.09E+00
3.2	2	1	–1.37E+01	–5.01E–10	1.13E+01
3.2	5	1	0.00E+00	0.00E+00	0.00E+00
3.2	10	1	0.00E+00	0.00E+00	0.00E+00
3.2	22	1	0.00E+00	0.00E+00	0.00E+00
10	1	1	–5.14E+00	–6.89E–04	4.80E+00
10	2	1	–9.39E+00	–3.35E–04	4.90E+00
10	5	1	0.00E+00	0.00E+00	0.00E+00
10	10	1	0.00E+00	0.00E+00	0.00E+00
10	22	1	0.00E+00	0.00E+00	0.00E+00
32	1	1	–2.10E+00	–1.05E–02	3.50E+00
32	2	1	–5.74E+00	–2.45E–03	4.10E+00
32	5	1	–1.33E+01	–3.73E–04	4.86E+00
32	10	1	0.00E+00	0.00E+00	0.00E+00
32	22	1	0.00E+00	0.00E+00	0.00E+00
100	1	1	6.23E–01	–3.44E–02	3.00E+00
100	2	1	–1.94E+00	–1.58E–02	3.30E+00
100	5	1	–6.44E+00	–1.16E–02	3.40E+00
100	10	1	0.00E+00	0.00E+00	0.00E+00
100	22	1	0.00E+00	0.00E+00	0.00E+00
320	1	1	3.14E+00	–7.57E–02	2.70E+00
320	2	1	1.18E+00	–5.14E–02	2.80E+00
320	5	1	–2.13E+00	–4.42E–02	2.80E+00
320	10	1	–8.30E+00	–1.01E–02	3.50E+00
320	22	1	0.00E+00	0.00E+00	0.00E+00
1000	1	1	5.32E+00	–1.48E–01	2.40E+00
1000	2	1	3.80E+00	–1.07E–01	2.50E+00
1000	5	1	8.81E–01	–7.59E–02	2.60E+00
1000	10	1	–2.76E+00	–3.01E–02	3.10E+00
1000	22	1	–7.66E+00	–5.66E–03	3.90E+00

Table A3: Parameters of the muon lateral distribution function (m^{-2}) using a form $exp\{a+b(lnr)^c\}$ with the distance r measured in meters

Energy (GeV)	Altitude (km)	cosθ	a	b	c
1	1	1	–3.98E+00	–7.02E–06	6.98E+00
1	2	1	–7.11E+00	–1.36E–07	8.71E+00
1	5	1	0.00E+00	0.00E+00	0.00E+00
1	10	1	0.00E+00	0.00E+00	0.00E+00
1	22	1	0.00E+00	0.00E+00	0.00E+00
3.2	1	1	–1.44E+00	–6.28E–04	4.93E+00
3.2	2	1	–3.14E+00	–1.10E–04	5.56E+00
3.2	5	1	–4.94E+00	–1.00E–04	5.33E+00
3.2	10	1	–7.53E+00	–1.30E–05	6.03E+00
3.2	22	1	–1.06E+01	–7.30E–06	6.04E+00
10	1	1	8.30E–01	–2.65E–02	3.06E+00
10	2	1	–6.84E–01	–7.42E–03	3.58E+00
10	5	1	–2.27E+00	–1.44E–03	4.26E+00
10	10	1	–3.91E+00	–4.76E–04	4.61E+00
10	22	1	–5.68E+00	–4.57E–04	4.41E+00
32	1	1	2.10E+00	–6.91E–02	2.57E+00
32	2	1	1.11E+00	–4.92E–02	2.65E+00
32	5	1	–1.98E–01	–2.72E–02	2.85E+00
32	10	1	–1.64E+00	–8.90E–03	3.31E+00
32	22	1	–3.16E+00	–1.85E–03	3.98E+00
100	1	1	2.93E+00	–6.44E–02	2.63E+00
100	2	1	2.15E+00	–4.97E–02	2.66E+00
100	5	1	1.14E+00	–4.51E–02	2.62E+00
100	10	1	1.59E–01	–4.61E–02	2.54E+00
100	22	1	–8.21E–01	–2.99E–02	2.74E+00
320	1	1	3.81E+00	–5.68E–02	2.75E+00
320	2	1	3.19E+00	–4.40E–02	2.76E+00
320	5	1	2.35E+00	–3.69E–02	2.75E+00
320	10	1	1.25E+00	–3.68E–02	2.67E+00
320	22	1	6.18E–01	–6.07E–02	2.40E+00
1000	1	1	4.83E+00	–8.11E–02	2.59E+00
1000	2	1	4.35E+00	–5.57E–02	2.68E+00
1000	5	1	3.60E+00	–3.88E–02	2.77E+00
1000	10	1	2.59E+00	–3.36E–02	2.75E+00
1000	22	1	1.87E+00	–4.34E–02	2.59E+00

Energy (GeV)	Altitude (km)	cosθ	a	b	c
1	1	0.9	–4.20E+00	–1.27E–05	6.62E+00
1	2	0.9	–8.16E+00	–1.13E–07	8.60E+00
1	5	0.9	0.00E+00	0.00E+00	0.00E+00
1	10	0.9	0.00E+00	0.00E+00	0.00E+00
1	22	0.9	0.00E+00	0.00E+00	0.00E+00
3.2	1	0.9	–1.67E+00	–4.54E–04	5.06E+00
3.2	2	0.9	–3.45E+00	–5.67E–05	5.85E+00
3.2	5	0.9	–5.51E+00	–2.85E–06	7.09E+00
3.2	10	0.9	–8.07E+00	–2.61E–07	7.98E+00
3.2	22	0.9	–1.14E+01	–1.16E–08	9.43E+00
10	1	0.9	6.39E–01	–2.21E–02	3.14E+00
10	2	0.9	–1.04E+00	–3.87E–03	3.89E+00
10	5	0.9	–2.62E+00	–7.79E–04	4.53E+00
10	10	0.9	–4.29E+00	–2.57E–04	4.88E+00
10	22	0.9	–5.98E+00	–2.45E–04	4.69E+00
32	1	0.9	1.92E+00	–7.02E–02	2.54E+00
32	2	0.9	9.09E–01	–4.46E–02	2.68E+00
32	5	0.9	–4.89E–01	–1.88E–02	3.02E+00
32	10	0.9	–1.81E+00	–7.68E–03	3.38E+00
32	22	0.9	–3.30E+00	–2.16E–03	3.89E+00
100	1	0.9	2.60E+00	–5.25E–02	2.71E+00
100	2	0.9	2.02E+00	–4.77E–02	2.67E+00
100	5	0.9	1.01E+00	–4.78E–02	2.57E+00
100	10	0.9	2.59E–02	–4.79E–02	2.51E+00
100	22	0.9	–1.14E+00	–1.81E–02	2.98E+00
320	1	0.9	3.43E+00	–4.35E–02	2.85E+00
320	2	0.9	3.09E+00	–4.27E–02	2.76E+00
320	5	0.9	2.10E+00	–3.22E–02	2.80E+00
320	10	0.9	1.20E+00	–4.66E–02	2.54E+00
320	22	0.9	5.81E–01	–6.90E–02	2.34E+00
1000	1	0.9	4.40E+00	–6.03E–02	2.71E+00
1000	2	0.9	4.28E+00	–5.44E–02	2.67E+00
1000	5	0.9	3.40E+00	–3.53E–02	2.79E+00
1000	10	0.9	2.43E+00	–3.50E–02	2.72E+00
1000	22	0.9	1.59E+00	–3.87E–02	2.63E+00

Energy (GeV)	Altitude (km)	cosθ	a	b	c
1	1	0.8	−4.57E+00	−2.01E−05	6.31E+00
1	2	0.8	−9.42E+00	−4.07E−07	7.77E+00
1	5	0.8	0.00E+00	0.00E+00	0.00E+00
1	10	0.8	0.00E+00	0.00E+00	0.00E+00
1	22	0.8	0.00E+00	0.00E+00	0.00E+00
3.2	1	0.8	−1.88E+00	−4.41E−04	5.03E+00
3.2	2	0.8	−3.76E+00	−2.02E−05	6.36E+00
3.2	5	0.8	−5.88E+00	−3.39E−06	6.96E+00
3.2	10	0.8	−8.83E+00	−2.96E−05	5.53E+00
3.2	22	0.8	−1.19E+01	−2.07E−05	5.59E+00
10	1	0.8	4.13E−01	−1.83E−02	3.22E+00
10	2	0.8	−1.22E+00	−3.41E−03	3.93E+00
10	5	0.8	−2.94E+00	−4.97E−04	4.72E+00
10	10	0.8	−4.55E+00	−2.54E−04	4.85E+00
10	22	0.8	−6.42E+00	−2.47E−04	4.62E+00
32	1	0.8	1.87E+00	−6.68E−02	2.55E+00
32	2	0.8	6.76E−01	−3.68E−02	2.76E+00
32	5	0.8	−7.40E−01	−1.60E−02	3.08E+00
32	10	0.8	−2.16E+00	−4.65E−03	3.61E+00
32	22	0.8	−3.53E+00	−2.23E−03	3.85E+00
100	1	0.8	2.76E+00	−6.41E−02	2.60E+00
100	2	0.8	1.88E+00	−4.63E−02	2.67E+00
100	5	0.8	8.20E−01	−4.60E−02	2.58E+00
100	10	0.8	−2.03E−01	−4.59E−02	2.52E+00
100	22	0.8	−1.07E+00	−3.10E−02	2.70E+00
320	1	0.8	3.64E+00	−5.34E−02	2.74E+00
320	2	0.8	2.96E+00	−3.94E−02	2.79E+00
320	5	0.8	1.96E+00	−3.25E−02	2.78E+00
320	10	0.8	9.11E−01	−3.96E−02	2.60E+00
320	22	0.8	7.44E−01	−1.28E−01	2.03E+00
1000	1	0.8	4.72E+00	−7.45E−02	2.60E+00
1000	2	0.8	4.18E+00	−5.06E−02	2.69E+00
1000	5	0.8	3.30E+00	−3.81E−02	2.74E+00
1000	10	0.8	2.12E+00	−3.02E−02	2.77E+00
1000	22	0.8	1.68E+00	−6.99E−02	2.33E+00

Energy (GeV)	Altitude (km)	cosθ	a	b	c
1	1	0.7	−4.93E+00	−3.26E−05	5.98E+00
1	2	0.7	−1.19E+01	−3.48E−09	7.65E+00
1	5	0.7	0.00E+00	0.00E+00	0.00E+00
1	10	0.7	0.00E+00	0.00E+00	0.00E+00
1	22	0.7	0.00E+00	0.00E+00	0.00E+00
3.2	1	0.7	−2.22E+00	−2.20E−04	5.35E+00
3.2	2	0.7	−3.99E+00	−6.72E−05	5.68E+00
3.2	5	0.7	−6.30E+00	−1.25E−05	6.24E+00
3.2	10	0.7	−9.84E+00	−9.06E−05	4.89E+00
3.2	22	0.7	0.00E+00	0.00E+00	0.00E+00
10	1	0.7	7.70E−02	−1.14E−02	3.44E+00
10	2	0.7	−1.51E+00	−2.53E−03	4.05E+00
10	5	0.7	−3.30E+00	−2.49E−04	5.04E+00
10	10	0.7	−4.88E+00	−2.26E−04	4.87E+00
10	22	0.7	−6.95E+00	−6.59E−05	5.21E+00
32	1	0.7	1.71E+00	−6.35E−02	2.56E+00
32	2	0.7	4.04E−01	−3.02E−02	2.84E+00
32	5	0.7	−1.06E+00	−1.05E−02	3.28E+00
32	10	0.7	−2.49E+00	−2.86E−03	3.83E+00
32	22	0.7	−3.89E+00	−1.07E−03	4.19E+00
100	1	0.7	2.64E+00	−6.26E−02	2.59E+00
100	2	0.7	1.68E+00	−4.39E−02	2.67E+00
100	5	0.7	5.93E−01	−4.49E−02	2.57E+00
100	10	0.7	−5.20E−01	−3.33E−02	2.67E+00
100	22	0.7	−1.53E+00	−1.65E−02	3.00E+00
320	1	0.7	3.54E+00	−5.21E−02	2.73E+00
320	2	0.7	2.85E+00	−4.06E−02	2.75E+00
320	5	0.7	1.66E+00	−2.96E−02	2.80E+00
320	10	0.7	6.17E−01	−3.48E−02	2.65E+00
320	22	0.7	1.63E−01	−6.28E−02	2.37E+00
1000	1	0.7	4.61E+00	−6.72E−02	2.63E+00
1000	2	0.7	4.07E+00	−4.88E−02	2.69E+00
1000	5	0.7	2.95E+00	−3.00E−02	2.83E+00
1000	10	0.7	1.73E+00	−2.22E−02	2.90E+00
1000	22	0.7	1.26E+00	−5.22E−02	2.46E+00

Energy (GeV)	Altitude (km)	cosθ	a	b	c
1	1	0.6	−5.62E+00	−2.93E−05	5.91E+00
1	2	0.6	0.00E+00	0.00E+00	0.00E+00
1	5	0.6	0.00E+00	0.00E+00	0.00E+00
1	10	0.6	0.00E+00	0.00E+00	0.00E+00
1	22	0.6	0.00E+00	0.00E+00	0.00E+00
3.2	1	0.6	−2.56E+00	−1.68E−04	5.43E+00
3.2	2	0.6	−4.30E+00	−8.90E−05	5.48E+00
3.2	5	0.6	−6.83E+00	−1.31E−05	6.18E+00
3.2	10	0.6	−1.13E+01	−9.78E−06	6.11E+00
3.2	22	0.6	0.00E+00	0.00E+00	0.00E+00
10	1	0.6	−3.26E−01	−6.49E−03	3.70E+00
10	2	0.6	−1.87E+00	−1.55E−03	4.27E+00
10	5	0.6	−3.66E+00	−1.93E−04	5.12E+00
10	10	0.6	−5.31E+00	−1.86E−04	4.91E+00
10	22	0.6	−7.57E+00	−3.33E−05	5.45E+00
32	1	0.6	1.48E+00	−5.55E−02	2.61E+00
32	2	0.6	6.50E−02	−2.29E−02	2.96E+00
32	5	0.6	−1.41E+00	−7.16E−03	3.45E+00
32	10	0.6	−2.88E+00	−1.72E−03	4.05E+00
32	22	0.6	−4.29E+00	−8.55E−04	4.26E+00
100	1	0.6	2.48E+00	−6.03E−02	2.59E+00
100	2	0.6	1.41E+00	−4.42E−02	2.64E+00
100	5	0.6	3.36E−01	−4.41E−02	2.56E+00
100	10	0.6	−6.75E−01	−3.75E−02	2.60E+00
100	22	0.6	−1.72E+00	−1.57E−02	3.01E+00
320	1	0.6	3.38E+00	−4.70E−02	2.76E+00
320	2	0.6	2.43E+00	−3.07E−02	2.86E+00
320	5	0.6	1.39E+00	−3.05E−02	2.76E+00
320	10	0.6	5.97E−01	−6.04E−02	2.37E+00
320	22	0.6	2.33E−01	−9.35E−02	2.17E+00
1000	1	0.6	4.45E+00	−5.95E−02	2.68E+00
1000	2	0.6	3.60E+00	−3.46E−02	2.83E+00
1000	5	0.6	2.62E+00	−2.57E−02	2.88E+00
1000	10	0.6	1.55E+00	−3.00E−02	2.73E+00
1000	22	0.6	1.28E+00	−8.27E−02	2.23E+00

Energy (GeV)	Altitude (km)	cosθ	a	b	c
1	1	0.5	−6.61E+00	−1.13E−05	6.19E+00
1	2	0.5	0.00E+00	0.00E+00	0.00E+00
1	5	0.5	0.00E+00	0.00E+00	0.00E+00
1	10	0.5	0.00E+00	0.00E+00	0.00E+00
1	22	0.5	0.00E+00	0.00E+00	0.00E+00
3.2	1	0.5	−3.00E+00	−6.39E−05	5.87E+00
3.2	2	0.5	−4.97E+00	−2.45E−05	6.06E+00
3.2	5	0.5	−7.98E+00	−3.61E−05	5.55E+00
3.2	10	0.5	0.00E+00	0.00E+00	0.00E+00
3.2	22	0.5	0.00E+00	0.00E+00	0.00E+00
10	1	0.5	−7.21E−01	−3.79E−03	3.94E+00
10	2	0.5	−2.37E+00	−5.83E−04	4.72E+00
10	5	0.5	−4.17E+00	−8.76E−05	5.46E+00
10	10	0.5	−5.76E+00	−8.57E−05	5.27E+00
10	22	0.5	−8.10E+00	−1.57E−05	5.80E+00
32	1	0.5	1.06E+00	−4.44E−02	2.69E+00
32	2	0.5	−4.00E−01	−1.35E−02	3.20E+00
32	5	0.5	−1.89E+00	−3.48E−03	3.78E+00
32	10	0.5	−3.24E+00	−1.12E−03	4.24E+00
32	22	0.5	−4.69E+00	−1.05E−03	4.10E+00
100	1	0.5	2.03E+00	−5.97E−02	2.55E+00
100	2	0.5	1.17E+00	−4.33E−02	2.63E+00
100	5	0.5	−1.59E−01	−2.70E−02	2.78E+00
100	10	0.5	−1.18E+00	−2.03E−02	2.88E+00
100	22	0.5	−2.06E+00	−1.25E−02	3.10E+00
320	1	0.5	2.72E+00	−3.58E−02	2.84E+00
320	2	0.5	2.18E+00	−2.98E−02	2.84E+00
320	5	0.5	1.04E+00	−2.95E−02	2.75E+00
320	10	0.5	3.37E−01	−5.79E−02	2.38E+00
320	22	0.5	−1.87E−01	−6.65E−02	2.33E+00
1000	1	0.5	3.68E+00	−4.23E−02	2.79E+00
1000	2	0.5	3.36E+00	−3.14E−02	2.85E+00
1000	5	0.5	2.27E+00	−2.30E−02	2.91E+00
1000	10	0.5	1.20E+00	−2.94E−02	2.71E+00
1000	22	0.5	8.04E−01	−5.94E−02	2.37E+00

7. REFERENCES

References to Chapter 1

References to this chapter are restricted to general documents which have been used as sources of information, with emphasis on VATLY publications, except for a few specific articles.

[1] P. Darriulat, Lectures on *Cosmic Rays, an Introduction*, Kathmandu 2010 and Ho Chi Minh City 2011, and references therein.

[2] The Pierre Auger Collaboration, Contributions to the 32nd International Cosmic Ray Conference, Beijing 2011, and references therein.

[3] D.K. The, *Diffusive Shock Acceleration of Cosmic Rays,* Master thesis defended at Hanoi University of Education, 2010, and references therein; D.K. The *et al.*, Comm. Phys. Vietnam, 21/3(2011) 199.

 [4] K. Greisen, Phys. Rev. Lett. 16 (1966) 748; G.T. Zatsepin and V.A. Kuzmin, Pisma Zh. Eksp. Teor. Fiz. 4 (1966) 114.

[5] R.J. Glauber and G. Matthiae, Nucl. Phys. B21 (1970) 135.

[6] P.N. Diep, *Contribution to the identification of primary ultra high energy cosmic rays using the Pierre Auger Observatory*, PhD thesis, 2010.

 [7] L. Alio, *Les Grandes Gerbes et L´effet LPM*, Dissertation presented at Hanoi National University, 2009; L.Alio *et al.*, Comm. Phys. Vietnam, 2(2010) 181.

References to Chapter 2

[8] L. Alio, *Les Grandes Gerbes et L´effet LPM*, Dissertation at Hanoi National University, 2009;

P.N. Diep, *Contribution to the identification of primary ultral high energy cosmic rays using the Pierre Auger Observatory*, PhD thesis, 2010;

L.Alio *et al.*, Comm. Phys. Vietnam, 2(2010) 181.

[9] Landau, L.D and Pomeranchuk, I.J., Dokl. Akad. Nauk. SSSR 92 535 (1953), Dokl. Akad. Nauk. SSSR 92, 735; These papers are available in English in The Collected Papers of L. D. Landau, Pergamon Press, 1965. Migdal, A. B., Phys. Rev. 103, 1811 (1956).

[10] D.H. Perkins, Phil. Mag. 46 (1955) 1146;

J. Iwadare, Phil. Mag. 3:31 (1958) 680.

[11] A.M. Hillas, Nucl. Phys. B (Proc. Suppl.) 52B (1997) 29 and references therein.

[12] Particle Data Group, S. Eidelman, et al., Physics Letters B592 (2004) 1.

[13] P. Sokolsky, Am. Inst. Phys. Conf. Proc. 433 (1998) 65.

References to Chapter 3

[14] L. Van Hove, Nucl. Phys. B9 (1969) 331 and Phys. Lett. 28B (1969) 429; see also *The Legacy of Leon Van Hove*, ed. A. Giovannini, World Scientific Series in 20th Century Physics, vol.28, November 2000.

[15] R.P. Feynman, Phys. Lett. (1969).

[16] L. Foa, Phys. Rep., 22 (1975) 1.

[17] G.J. Alner et al., Phys. Rep. 154/5-6 (1987) 247; R.E. Ansorge et al., Z. Phys. C 43 (1989) 357.

[18] *The Creation of QCD and the Effective Energy, in honour of A.Zichichi,* ed. V.N. Gribov, G. 't Hooft, G. Veneziano and V.F. Weisskopf, Wotld Scientific Series in 20th Century Physics, Vol. 25, 2000.

[19] J.N. Capdevielle, J. Phys. G : Nucl. Part. Phys. 15 (1989) 909.

[20] David J. Gross and Frank Wilczek, Phys. Rev. Lett. 30 (1973) 1343;

Phys. Rev. D8 (1973) 3633 and Phys. Rev. D9 (1974) 980;

H. Fritzsch, Murray Gell-Mann and H. Leutwyler, Phys. Lett. 47B (1973) 368;

David J. Gross, *Asymptotic freedom, Confinement and QCD, History of Original Ideas and Basic Discoveries in Particle Physics*;

H. B. Newman and T. Ypsilantis editors, NATO ASI series, B352 (1994) 75;

Gerard 't Hooft, *Gauge Theory and Renormalization;*

H. B. Newman and T. Ypsilantis editors, *History of Original Ideas and Basic Discoveries in Particle Physics*, NATO ASI series, B352 (1994) 37;

L.N. Lipatov Editor, *The Creation of Quantum Chromodynamics, The Creation of Quantum Chromodynamics and the Effective Energy*, World Scientific Series in XXth century Physics, Volume 25.

[21] A. Capella, Surveys in High Energy Physics, 16/3-4 (2001) 175);

J. Ranft, Phys. Rev. D51 (1995) 64;

P. Aurenche et al., Phys. Rev. D45 (1992) 92.

[22] D. Amati, S.Fubini and A. Stranghellini, Nuovo Cimento 26 (1962) 896; G.F. Chew and A. Pignotti, Phys.Rev.176 (1968) 2112; G.F. Chew, M.L. Goldberger and F. Low, Phys. Rev. Lett. 22 (1969) 208; D. Amati, L. Caneschi and M. Ciafaloni, Nucl. Phys. B62 (1973) 173.

[23] D. Heck *et al, Corsika: A Monte Carlo code to simulate extensive air showers*, Forschungszentrum Karlsruhe, Wissenschaftliche Berichte FZKA 6019 (1998).

[24] R.J. Glauber and G. Matthiae, Nucl. Phys. B21 (1970) 135.

[25] A. Klar and J. Hüfner, Phys. Rev. D31 (1985) 491.